A&A 536, A19 (2011)
DOI: 10.1051/0004-6361/201116479

Astronomy & Astrophysics
Special feature

Planck early results

Planck early results. XIX. All-sky temperature and dust optical depth from *Planck* and IRAS. Constraints on the "dark gas" in our Galaxy⋆

Planck Collaboration: P. A. R. Ade[75], N. Aghanim[50], M. Arnaud[62], M. Ashdown[60,4], J. Aumont[50], C. Baccigalupi[73], A. Balbi[31], A. J. Banday[79,7,67], R. B. Barreiro[57], J. G. Bartlett[3,58], E. Battaner[81], K. Benabed[51], A. Benoît[49], J.-P. Bernard[79,7], M. Bersanelli[28,44], R. Bhatia[5], J. J. Bock[58,8], A. Bonaldi[40], J. R. Bond[6], J. Borrill[66,76], F. R. Bouchet[51], F. Boulanger[50], M. Bucher[3], C. Burigana[43], P. Cabella[31], J.-F. Cardoso[63,3,51], A. Catalano[3,61], L. Cayón[21], A. Challinor[54,60,10], A. Chamballu[47], L.-Y Chiang[53], C. Chiang[20], P. R. Christensen[70,32], D. L. Clements[47], S. Colombi[51], F. Couchot[65], A. Coulais[61], B. P. Crill[58,71], F. Cuttaia[43], T. M. Dame[37], L. Danese[73], R. D. Davies[59], R. J. Davis[59], P. de Bernardis[27], G. de Gasperis[31], A. de Rosa[43], G. de Zotti[40,73], J. Delabrouille[3], J.-M. Delouis[51], F.-X. Désert[46], C. Dickinson[59], K. Dobashi[15], S. Donzelli[44,55], O. Doré[58,8], U. Dörl[67], M. Douspis[50], X. Dupac[35], G. Efstathiou[54], T. A. Enßlin[67], H. K. Eriksen[55], E. Falgarone[61], F. Finelli[43], O. Forni[79,7], P. Fosalba[52], M. Frailis[42], E. Franceschi[43], Y. Fukui[19], S. Galeotta[42], K. Ganga[3,48], M. Giard[79,7], G. Giardino[36], Y. Giraud-Héraud[3], J. González-Nuevo[73], K. M. Górski[58,83], S. Gratton[60,54], A. Gregorio[29], I. A. Grenier[62], A. Gruppuso[43], F. K. Hansen[55], D. Harrison[54,60], G. Helou[8], S. Henrot-Versillé[65], D. Herranz[57], S. R. Hildebrandt[8,64,56], E. Hivon[51], M. Hobson[4], W. A. Holmes[58], W. Hovest[67], R. J. Hoyland[56], K. M. Huffenberger[82], A. H. Jaffe[47], W. C. Jones[20], M. Juvela[18], A. Kawamura[19], E. Keihänen[18], R. Keskitalo[58,18], T. S. Kisner[66], R. Kneissl[34,5], L. Knox[23], H. Kurki-Suonio[18,38], G. Lagache[50], J.-M. Lamarre[61], A. Lasenby[4,60], R. J. Laureijs[36], C. R. Lawrence[58], S. Leach[73], R. Leonardi[35,36,24], C. Leroy[50,79,7], P. B. Lilje[55,9], M. Linden-Vørnle[12], M. López-Caniego[57], P. M. Lubin[24], J. F. Macías-Pérez[64], C. J. MacTavish[60], B. Maffei[59], D. Maino[28,44], N. Mandolesi[43], R. Mann[74], M. Maris[42], P. Martin[6], E. Martínez-González[57], S. Masi[27], S. Matarrese[26], F. Matthai[67], P. Mazzotta[31], P. McGehee[48], P. R. Meinhold[24], A. Melchiorri[27], L. Mendes[35], A. Mennella[28,42], M.-A. Miville-Deschênes[50,6], A. Moneti[51], L. Montier[79,7], G. Morgante[43], D. Mortlock[47], D. Munshi[75,54], A. Murphy[69], P. Naselsky[70,32], P. Natoli[30,2,43], C. B. Netterfield[14], H. U. Nørgaard-Nielsen[12], F. Noviello[50], D. Novikov[47], I. Novikov[70], I. J. O'Dwyer[58], T. Onishi[16], S. Osborne[78], F. Pajot[50], R. Paladini[77,8], D. Paradis[79,7], F. Pasian[42], G. Patanchon[3], O. Perdereau[65], L. Perotto[64], F. Perrotta[73], F. Piacentini[27], M. Piat[3], S. Plaszczynski[65], E. Pointecouteau[79,7], G. Polenta[2,41], N. Ponthieu[50], T. Poutanen[38,18,1], G. Prézeau[8,58], S. Prunet[51], J.-L. Puget[50], W. T. Reach[80], M. Reinecke[67], C. Renault[64], S. Ricciardi[43], T. Riller[67], I. Ristorcelli[79,7], G. Rocha[58,8], C. Rosset[3], M. Rowan-Robinson[47], J. A. Rubiño-Martín[56,33], B. Rusholme[48], M. Sandri[43], D. Santos[64], G. Savini[72], D. Scott[17], M. D. Seiffert[58,8], P. Shellard[10], G. F. Smoot[22,66,3], J.-L. Starck[62,11], F. Stivoli[45], V. Stolyarov[4], R. Stompor[3], R. Sudiwala[75], J.-F. Sygnet[51], J. A. Tauber[36], L. Terenzi[43], L. Toffolatti[13], M. Tomasi[28,44], J.-P. Torre[50], M. Tristram[65], J. Tuovinen[68], G. Umana[39], L. Valenziano[43], P. Vielva[57], F. Villa[43], N. Vittorio[31], L. A. Wade[58], B. D. Wandelt[51,25], A. Wilkinson[59], D. Yvon[11], A. Zacchei[42], and A. Zonca[24]

(Affiliations can be found after the references)

Received 9 January 2011 / Accepted 17 May 2011

ABSTRACT

An all sky map of the apparent temperature and optical depth of thermal dust emission is constructed using the *Planck*-HFI (350 μm to 2 mm) and IRAS (100 μm) data. The optical depth maps are correlated with tracers of the atomic (H I) and molecular gas traced by CO. The correlation with the column density of observed gas is linear in the lowest column density regions at high Galactic latitudes. At high $N_{\rm H}$, the correlation is consistent with that of the lowest $N_{\rm H}$, for a given choice of the CO-to-H_2 conversion factor. In the intermediate $N_{\rm H}$ range, a departure from linearity is observed, with the dust optical depth in excess of the correlation. This excess emission is attributed to thermal emission by dust associated with a dark gas phase, undetected in the available H I and CO surveys. The 2D spatial distribution of the dark gas in the solar neighbourhood ($|b_{\rm II}| > 10°$) is shown to extend around known molecular regions traced by CO. The average dust emissivity in the H I phase in the solar neighbourhood is found to be $\tau_{\rm D}/N_{\rm H}^{\rm tot} = 5.2 \times 10^{-26}$ cm^2 at 857 GHz. It follows roughly a power law distribution with a spectral index $\beta = 1.8$ all the way down to 3 mm,

⋆ Corresponding author: J.-P. Bernard,
e-mail: Jean-Philippe.Bernard@cesr.fr

although the SED flattens slightly in the millimetre. Taking into account the spectral shape of the dust optical depth, the emissivity is consistent with previous values derived from FIRAS measurements at high latitudes within 10%. The threshold for the existence of the dark gas is found at $N_{\rm H}^{\rm tot} = (8.0 \pm 0.58) \times 10^{20}$ H cm^{-2} ($A_V = 0.4$ mag). Assuming the same high frequency emissivity for the dust in the atomic and the molecular phases leads to an average $X_{\rm CO} = (2.54 \pm 0.13) \times 10^{20}$ H$_2$ cm^{-2}/(K km s^{-1}). The mass of dark gas is found to be 28% of the atomic gas and 118% of the CO emitting gas in the solar neighbourhood. The Galactic latitude distribution shows that its mass fraction is relatively constant down to a few degrees from the Galactic plane. A possible explanation for the dark gas lies in a dark molecular phase, where H_2 survives photodissociation but CO does not. The observed transition for the onset of this phase in the solar neighbourhood ($A_V = 0.4$ mag) appears consistent with recent theoretical predictions. It is also possible that up to half of the dark gas could be in atomic form, due to optical depth effects in the H I measurements.

Key words. dust, extinction – ISM: clouds – evolution – solar neighborhood – Galaxy: general – submillimeter: ISM

1. Introduction

The matter that forms stars, that is left over after star formation, or that has never experienced star formation comprises the interstellar medium (ISM). The life-cycle and the duration of the various observable phases remains largely unknown, because the nature of the diffuse ISM is difficult to discern, owing to its low temperatures and large angular scales.

The distribution of diffuse interstellar gas, by which we mean gas not in gravitationally-bound structures and not in the immediate vicinity of active star-formation regions, has primarily been assessed using the 21-cm hyperfine line of atomic hydrogen. That line is easily excited by collisions and is optically thin for gas with temperature $T_K > 50$ K and velocity dispersion $\delta V > 10$ km s^{-1} as long as the column density is less than 9×10^{21} cm^{-2} (Kulkarni & Heiles 1988). Such conditions are typical of the diffuse ISM pervaded by the interstellar radiation field (ISRF), because photoelectric heating from grain surfaces keeps the gas warm ($T > 50$ K), and observed velocity dispersions (presumably due to turbulence) are typically >10 km s^{-1}. Based on the observed dust extinction per unit column density, $N({\rm HI})/A_V = 1.9 \times 10^{21}$ cm^{-2} mag^{-1} (Bohlin et al. 1978), the upper column density for optically thin 21-cm lines corresponds to visible extinctions $A_V < 4.7$. Thus the 21-cm line is expected to trace diffuse, warm atomic gas accurately throughout the diffuse ISM, except for lines of sight that are visibly opaque or are particularly cold.

Molecular gas is typically traced by the 2.6-mm ^{12}CO($J = 1 \rightarrow 0$) rotational line in emission, which, like the 21-cm H I line, can be easily excited because it involves energy levels that can be obtained by collisions. The CO emission line, however, is commonly optically thick, due to its high radiative transition rate. In the limit where the lines are optically thick, the primary information determining the amount of molecular gas in the beam is the line width. If the material is gravitationally bound, then the virial mass is measured and CO can be used as a tracer of molecular mass. It is common astronomical practice to consider the velocity-integrated CO line intensity as measuring the molecular column density, with the implicit assumption that the material is virialized and the mass of the virialized structures is being measured (e.g. Dickman et al. 1986; Heyer et al. 2001). In the diffuse ISM, these conditions typically do not apply. On a physical scale of R (measured in parsecs), interstellar material is only virialized if its column density $N > 5.2 \times 10^{21}\, \delta V^2\, R^{-1}$ cm^{-2} where δV is the velocity dispersion (measured in km s^{-1}). Thus the diffuse ISM is typically gravitationally unbound, invalidating the usage of CO as a virial tracer of the molecular gas mass, except in very compact regions or in regions that are visibly opaque. Although CO can emit in gas with low density, the critical density required for collisional equilibrium is of order 10^3 cm^{-3}, which further complicates the usage of CO as a tracer. This again is not typical of the diffuse ISM.

To measure the amount and distribution of the molecular ISM, as well as the cold atomic ISM, other tracers of the interstellar gas are required. At least three tracers have been used in the past. These are UV absorption in Werner bands of H_2, infrared emission from dust, and γ-ray emission from pion production due to cosmic-rays colliding with interstellar nucleons. The UV absorption is exceptionally sensitive to even very low H_2 column densities of 10^{17} cm^{-2}. Using *Copernicus* (Savage et al. 1977) and FUSE data, atomic and molecular gas could be measured simultaneously on the sightlines to UV-bright stars and some galaxies. A survey at high Galactic latitudes with FUSE showed that the molecular fraction of the ISM, $f(H_2) \equiv 2N(H_2)/[2N(H_2) + N({\rm HI})] < 10^{-3}$ for lines of sight with total column density less than 10^{20} cm^{-2}, but there is a tremendous dispersion from 10^{-4} to 10^{-1} for higher-column density lines of sight (Wakker 2006). Since UV-bright sources are preferentially found towards the lowest-extinction sightlines, an accurate average $f(H_2)$ is extremely difficult to determine from the stellar absorption measurements. Along lines of sight toward AGNs behind diffuse interstellar clouds, Gillmon & Shull (2006) found molecular hydrogen fractions of 1–30% indicating significant molecular content even for low-density clouds.

The dust column density has been used as a total gas column density tracer, with the assumption that gas and dust are well mixed. The possibility that dust traces the column density better than H I and CO was recognized soon after the first all-sky infrared survey by IRAS, which for the first time revealed the distribution of dust on angular scales down to 5′. Molecular gas without CO was inferred from comparing IRAS 100 μm surface brightness to surveys of the 21-cm and 2.6-mm lines of H I and CO on 9′ or degree scale by de Vries et al. (1987); Heiles et al. (1988); Blitz et al. (1990). At 3′ scale using Arecibo, the cloud G236+39 was found to have significant infrared emission unaccounted for by 21-cm or 2.6-mm lines, with a large portion of the cloud being possibly H_2 with CO emission below detection threshold (Reach et al. 1994). Meyerdierks & Heithausen (1996) also detected IR emission surrounding the Polaris flare in excess of what was expected from the H I and CO emission, which they attributed to diffuse molecular gas. The all sky far-infrared observations by COBE – DIRBE (Hauser et al. 1998) made it possible to survey the molecular gas not traced by H I or CO at the 1° scale (Reach et al. 1998). This revealed numerous "infrared excess" clouds, many of which were confirmed as molecular after detection of faint CO with NANTEN (Onishi et al. 2001). Finally, there are also indications of more dust emission than seen in nearby external galaxies such as the Large Magellanic Cloud (Bernard et al. 2008; Roman-Duval et al. 2010) and the Small Magellanic Cloud (Leroy et al. 2007). This suggests that large fractions of the gas masses of these galaxies are not detected using standard gas tracers.

The γ-rays from the ISM provide an independent tracer of the total nucleon density. As was the case with the dust column

density, the γ-ray inferred nucleon column density appears to show an extra component of the ISM not associated with detected 21-cm or 2.6-mm emission; this extra emission was referred to as "dark gas" (e.g. Grenier et al. 2005; Abdo et al. 2010), a term we will adopt in this paper to describe interstellar material beyond what is traced by H I and CO emission. Grenier et al. (2005) inferred dark gas column densities of order 50% of the total column density toward locations with little or beyond detection threshold CO emission, and general consistency between infrared and γ-ray methods of detection. Recent observations using *Fermi* have significantly advanced this method, allowing γ-ray emission to be traced even by the high-latitude diffuse ISM. In the Cepheus, Cassiopeia, and Polaris Flare clouds, the correlated excess of dust and γ rays yields dark gas masses that range from 40% to 60% of the CO-bright molecular mass (Abdo et al. 2010).

Theoretical work predicts a dark molecular gas layer in regions where the balance between photodissociation and molecular formation allows H_2 to form in significant quantity while in the gas-phase C remains atomic or ionized (Wolfire et al. 2010; Glover et al. 2010). In this paper we describe new observations made with *Planck*[1] (Planck Collaboration 2011a) that trace the distribution of submillimeter emission at 350 μm and longer wavelengths. In combination with observations up to 100 μm wavelength by IRAS and COBE – DIRBE , we are uniquely able to trace the distribution of interstellar dust with temperatures down to $\sim$ 10 K. The surface brightness sensitivity of *Planck*, in particular on angular scales of 5′ to 7°, is unprecedented. Because we can measure the dust optical depth more accurately by including the *Planck* data, we can now reassess the relationship between dust and gas, and relate it to previous infrared and independent UV and γ-ray results, and compare it to theoretical explanations to determine just how important the dark gas is for the evolution of the ISM.

2. Observations

2.1. Planck data

The *Planck* first mission results are presented in Planck Collaboration (2011a) and the in-flight performances of the two focal plane instruments HFI (High Frequency Instrument) and LFI (Low Frequency Instrument) are given in Planck HFI Core Team (2011a) and Mennella et al. (2011) respectively. The data processing and calibration of the HFI and LFI data used here is described in Planck HFI Core Team (2011b) and Zacchei et al. (2011) respectively.

Here we use only the HFI (DR2 release) data, the processing and calibration of which are described in Planck HFI Core Team (2011b). In this data the CMB component was identified and subtracted through a needlet internal linear combination (NILC) (Planck HFI Core Team 2011b).

We use the internal variance on intensity ($\sigma_{\rm II}^2$) estimated during the *Planck* data processing and provided with the *Planck*-HFI data, which we assume represents the white noise on the intensity. Note that this variance is inhomogeneous over the sky, owing to the *Planck* scanning strategy (Planck Collaboration 2011a), with lower values in the *Planck* deep fields near the ecliptic poles. We have checked that, within a small factor (<2), the data variance above is consistent with "Jack-Knife" maps obtained from differencing the two halves of the *Planck* rings. We also use the absolute uncertainties due to calibration uncertainties given in Planck HFI Core Team (2011b) for HFI and summarized in Table 1. We note that, for a large scale analysis such as carried out here, variances contribute to a small fraction of the final uncertainty resulting from combining data over large sky regions, so that most of the final uncertainty is due to absolute uncertainties.

[1] *Planck* (http://www.esa.int/*Planck*) is a project of the European Space Agency (ESA) with instruments provided by two scientific consortia funded by ESA member states (in particular the lead countries: France and Italy) with contributions from NASA (USA), and telescope reflectors provided in a collaboration between ESA and a scientific consortium led and funded by Denmark.

Table 1. Characteristics of the data used in this study.

Data	$\lambda_{\rm ref}$ [μm]	$\nu_{\rm ref}$ [GHz]	θ [arcmin]	$\sigma_{\rm II}$ [MJy/sr]	$\sigma_{\rm abs}$ [%]
IRAS	100.0	2998	4.30	0.06	13.6[†‡]
HFI	349.8	857	3.67	0.12[♭]	7%
HFI	550.1	545	3.80	0.12[♭]	7%
HFI	849.3	353	4.43	0.08[♭]	$\lesssim$2%
HFI	1381.5	217	4.68	0.08[♭]	$\lesssim$2%
HFI	2096.4	143	7.04	0.08[♭]	$\lesssim$2%
HFI	2997.9	100	9.37	0.07[♭]	$\lesssim$2%
Data	**line**	$\lambda_{\rm ref}$ [μm]	θ [arcmin]	σ [K km s^{-1}]	$\sigma_{\rm abs}$ [%]
LAB	H_I	21 cm	36.0	1.70[♯]	10.0
DHT	^{12}CO	2.6 mm	8.8	1.20	24.0
Dame	^{12}CO	2.6 mm	8.4	0.6	24.0
NANTEN	^{12}CO	2.6 mm	2.6	1.20	10.0

Notes. $\lambda_{\rm ref}$ and $\nu_{\rm ref}$ are the reference wavelength and frequencies of the photometric channels. θ is the beam FWHM. $\sigma_{\rm II}$ and $\sigma_{\rm abs}$ are the data variance and the absolute calibration uncertainty respectively. [†] Assumed to be for the average IRAS coverage. $\sigma_{\rm II}$ computed by rescaling this value to actual coverage. [(‡)] From Miville-Deschênes & Lagache (2005). [(♭)] 1σ average value in one beam scaled from Planck HFI Core Team (2011b). We actually use internal variance maps for $\sigma_{\rm II}$. [(♯)] 1σ average value. We actually use a map of the uncertainties (see Sect. 2.2.1).

2.2. Ancillary data

2.2.1. HI data

In order to trace the atomic medium, we use the LAB (Leiden/Argentine/Bonn) survey which contains the final data release of observations of the H I 21-cm emission line over the entire sky (Kalberla et al. 2005). This survey merged the Leiden/Dwingeloo Survey (Hartmann & Burton 1997) of the sky north at $\delta > -30°$ with the IAR (Instituto Argentino de Radioastronomia) Survey (Arnal et al. 2000; Bajaja et al. 2005) of the Southern sky at $\delta < -25°$. The angular resolution and the velocity resolution of the survey are ~0.6° and ~1.3 km s^{-1}. The LSR velocity range $-450 < V_{\rm LSR} < 400$ km s^{-1} is fully covered by the survey with 891 channels with a velocity separation of $\Delta V_{\rm ch} = 1.03$ km s^{-1}.

The data were corrected for stray radiation at the Institute for Radioastronomy of the University of Bonn. The rms brightness-temperature noise of the merged database is slightly lower in the southern sky than in the northern sky, ranging over 0.07–0.09 K. Residual uncertainties in the profile wings, due to defects in the correction for stray radiation, are for most of the data below a level of 20 to 40 mK. We integrated the LAB data in the

velocity range $-400 < V_{\rm LSR} < 400\,{\rm km\,s^{-1}}$ to produce an all sky map of the H I integrated intensity ($W_{\rm HI}$), which was finally projected into the HEALPix pixelisation scheme using the method described in Sect. 2.3.1.

We estimate the noise level of the $W_{\rm HI}$ map as $\Delta T_{\rm rms}\Delta V_{\rm ch}\sqrt{N_{\rm ch}}$ where $N_{\rm ch}$(=777) is the number of channels used for the integration, and $\Delta T_{\rm rms}$ is the rms noise of the individual spectra measured in the emission-free velocity range mainly in $-400 < V_{\rm LSR} < 350\,{\rm km\,s^{-1}}$. The resulting noise of the $W_{\rm HI}$ map is mostly less than $\sim$2.5 K km s^{-1} all over the sky with an average value of $\sim$1.7 K km s^{-1}, except for some limited positions showing somewhat larger noise ($\sim$10 K km s^{-1}).

2.2.2. CO data

In order to trace the spatial distribution of the CO emission, we use a combination of 3 large scale surveys in the ^{12}CO($J = 1 \rightarrow 0$) line.

In the Galactic plane, we use the Dame et al. (2001) survey obtained with the CfA telescope in the north and the CfA-Chile telescope in the south, referred to here as DHT (Dame, Hartmann and Thaddeus). These data have an angular resolution of 8.4′ ± 0.2′ and 8.8′ ± 0.2′ respectively. The velocity coverage and the velocity resolution for these data vary from region to region on the sky, depending on the individual observations composing the survey. The most heavily used spectrometer is the 500 kHz filter bank providing a velocity coverage and resolution of 332 km s^{-1}and 1.3 km s^{-1}, respectively. Another 250 kHz filter bank providing the 166 km s^{-1}coverage and 0.65 km s^{-1}resolution was also frequently used . The rms noises of these data are suppressed down to 0.1–0.3 K (for details, see their Table 1). The data cubes have been transformed into the velocity-integrated intensity of the line ($W_{\rm CO}$) by integrating the velocity range where the CO emission is significantly detected using the moment method proposed by Dame (2011). The noise level of the $W_{\rm CO}$ map is typically $\sim$1.2 K km s^{-1}, but it varies by a factor of a few depending on the integration range used.

We also use the unpublished high latitude survey obtained using the CfA telescope (Dame et al. 2010, priv. comm.). This survey is still on-going and covers the northern sky up to latitudes as high as $|b_{\rm II}| = 70°$ which greatly increases the overall sky coverage. The noise level of the CO spectra are suppressed to $\sim$0.18 K for the 0.65 km s^{-1}velocity resolution, and the total CO intensity was derived by integrating typically 10–20 velocity channels, which results in a noise level of 0.4–0.6 K km s^{-1}.

Finally, we combined the above surveys with the NANTEN ^{12}CO($J = 1 \rightarrow 0$) survey obtained from Chile. This survey complements some of the intermediate Galactic latitudes not covered by the Dame et al. (2001) maps with an angular resolution of 2.6′. Most of the survey along the Galactic plane has a velocity coverage of $\sim$650 km s^{-1}with a wide band spectrometer, but a part of the survey has a coverage of $\sim$100 km s^{-1}with a narrow band spectrometer. The noise level achieved was 0.4–0.5 K at a velocity resolution of 0.65 km s^{-1}. The CO spectra were sampled with the 2′ grid in the Galactic centre, and with the 4′ and 8′ grid along the Galactic plane in the latitude range $|b| < 5°$and $|b| > 5°$, respectively. The integrated intensity maps were obtained by integrating over the whole velocity range, excluding regions of the spectra where no emission is observed. The resulting rms noise in the velocity-integrated intensity map varies depending on the width of the emission. This survey along the Galactic plane is still not published in full, but parts of the survey have been analyzed (e.g. Fukui et al. 1999; Matsunaga et al. 2001; Mizuno & Fukui 2004). A large amount of the sky at intermediate Galactic latitude toward the nearby clouds is also covered with a higher velocity resolution of $\sim$0.1 km s^{-1} with a narrow band spectrometer with a $\lesssim$100 km s^{-1} band (e.g. Onishi et al. 1999; Kawamura et al. 1999; Mizuno et al. 2001). The velocity coverage, the grid spacing, and the noise level for these data vary, depending on the characteristics of the individual clouds observed, but the quality of the data is high enough to trace the total CO intensity of the individual clouds.

The three surveys were repixelised into the HEALPix pixelisation scheme (Górski et al. 2005) with the appropriate pixel size to ensure Shannon sampling of the beam (Nside = 2048 for the NANTEN2 survey and Nside = 1024 for the CfA surveys, where the Nside HEALPix parameter controls the number of pixels on the celestial sphere defined as $N_{\rm pix} = 12 \times {\rm Nside}^2$) using the procedure described in Sect. 2.3.1.

Each survey was smoothed to a common resolution of 8.8′ through convolution with a Gaussian with kernel size adjusted to go from the original resolution of each survey to a goal resolution of 8.8′, using the smoothing capabilities of the HEALPix software.

We checked the consistency of the different surveys in the common region observed with NANTEN and CfA. We found a reasonably good correlation between the two but a slope indicating that the NANTEN survey yields 24% larger intensities than the CfA values. The origin of this discrepancy is currently unknown. We should note that the absolute intensity scale in CO observations is not highly accurate as noted often in the previous CO papers. Since the CfA survey covers most of the regions used in this paper and has been widely used for calibrating the H_2 mass calibration factor $X_{\rm CO}$, in particular by several generations of gamma ray satellites, we assumed the CfA photometry when merging the data, and therefore rescaled the NANTEN data down by 24% before merging. Note that this an arbitrary choice. The implications on our results will be discussed in Sect. 6.1.

The 3 surveys were then combined into a single map. In doing so, data from different surveys falling into the same pixel were averaged using σ^2 as a weight. The resulting combined map was then smoothed to the resolution appropriate to this study. Note that part of the NANTEN and CfA surveys are undersampled. However, this has very minimal effect on the results presented here since the small data gaps are filled while smoothing the CO data to the coarser resolution of the H I data (0.6°). The resulting CO integrated intensity map is shown in Fig. 1.

2.2.3. IR data

We use the IRIS (Improved Reprocessing of the IRAS Survey) IRAS 100 μm data (see Miville-Deschênes & Lagache 2005) in order to constrain the dust temperature. The data, provided in the original format of individual tiles spread over the entire sky were combined into the HEALPix pixelisation using the method described in Sect. 2.3.1 at a HEALPix resolution (Nside = 2048 corresponding to a pixel size of 1.7′). The IRAS coverage maps were also processed in the same way. We assume the noise properties given in Miville-Deschênes & Lagache (2005) and given in Table 1. The noise level of 0.06 MJy sr^{-1} at 100 μm was assumed to represent the average data noise level and was appropriately multiplied by the coverage map to lead to the pixel variance of the data.

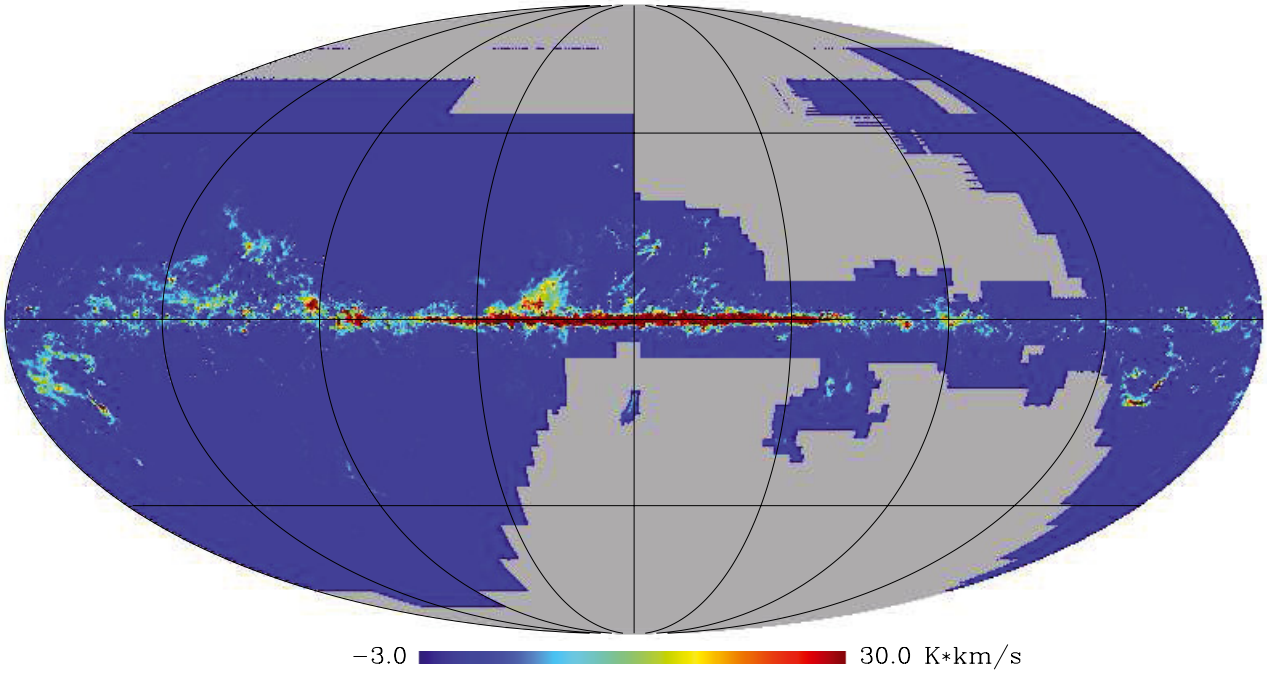

Fig. 1. Map of the ^{12}CO($J = 1 \rightarrow 0$) integrated intensity used in this paper combining the Dame et al. (2001) and high latitude survey and the NANTEN survey. The data shown cover 62.8% of the sky. The map is shown at a common resolution of all the sub-surveys of 8.8′. Many small clouds at high latitude are not visible in this rendering of the data.

2.3. Additional data processing

2.3.1. Common angular resolution and pixelisation

The individual maps are then combined into HEALPix using the intersection surface as a weight. This procedure was shown to preserve photometry accuracy.

The ancillary data described in Sect. 2.2 were brought to the HEALPix pixelisation, using a method where the surface of the intersection between each HEALPix pixel with each FITS pixel of the survey data is computed and used as a weight to regrid the data. The HEALPix resolution was chosen so as to match the Shannon sampling of the original data at resolution θ, with a HEALPix resolution set so that the pixel size is $<\theta/2.4$. The ancillary data and the description of their processing will be presented in Paradis et al. (in prep.).

All ancillary data were then smoothed to an appropriate resolution by convolution with a Gaussian smoothing function with appropriate FWHM using the smoothing HEALPix function, and were brought to a pixel size matching the Shannon sampling of the final resolution.

2.3.2. Background levels

Computing the apparent temperature and optical depth of thermal dust over the whole sky requires accurate subtraction of any offset (I_ν^0) in the intensity data, either of instrumental or astrophysical origin. Although both the IRIS and the *Planck*-HFI data used in this study have been carefully treated with respect to residual offsets during calibration against the FIRAS data, the data still contains extended sources of emission unrelated to the Galactic emission, such as the Cosmic InfraRed Background (CIB) signal (Miville-Deschênes et al. 2002; Planck Collaboration 2011n) or zodiacal light which could affect the determination of the dust temperature and optical depth at low surface brightness.

In order to estimate the above data offsets, we first compute the correlation between IR and H I emission in a reference region such that $|b_{\rm II}| > 20^\circ$ and $N_{\rm H}^{\rm HI} < 1.2 \times 10^{21}\,{\rm H\,cm^{-2}}$. This was done using the IDL *regress* routine and iterative removal of outliers. The derived dust emissivities ($(I_\nu/N_{\rm H})^{\rm ref}$) are given in Table 2. The uncertainties given are those derived from the correlation using the data variance as the data uncertainty. The derived emissivities are in agreement with the ensemble average of the values found for the local H I velocities in Planck Collaboration (2011t) (see their Table 2) for individual smaller regions at high Galactic latitude, within the uncertainties quoted in Table 2. Note that these emissivities are used only to derive the offsets in this study.

We then select sky pixels with HI column densities $N_{\rm H}^{\rm HI} < 2.0 \times 10^{19}\,{\rm H\,cm^{-2}}$ and compute the average H I column density in this region to be $N_{\rm H}^{\rm low} = 1.75 \times 10^{19}\,{\rm H\,cm^{-2}}$. The offsets are then computed assuming that the dust emissivity in this region is the same as in the reference region, ie,

$$I_\nu^0 = I_\nu^{\rm low} - (I_\nu/N_{\rm H})^{\rm ref} \times N_{\rm H}^{\rm low} \quad (1)$$

where $I_\nu^{\rm low}$ is the average brightness at frequency ν in the sky region with $N_{\rm H}^{\rm HI} < 2.0 \times 10^{19}\,{\rm H\,cm^{-2}}$.

The offset values derived from the above procedure are given in Table 2 and were subtracted from the maps used in the rest of this analysis. The offset uncertainties also listed in Table 2 were derived from the emissivity uncertainties propagated to the offset values through Eq. (1). When subtracting the above offsets from the IRAS and *Planck* intensity maps, the data variances were combined with the offset uncertainties in order to reflect uncertainty on the offset determination. Note that, for consistency and future use, Table 2 also lists emissivities and offset values for FIR-mm datasets not used in this study. Note also that these offsets for *Planck* data are not meant to replace the official values provided with the data, since they suppress any large scale emission not correlated with H I, whatever their origin.

Table 2. Thermal dust emissivity derived from the correlation with H_I emission in the reference region with $|b_{II}| > 20°$ and $N_H^{HI} < 1.2 \times 10^{21}$ H cm^{-2} ($(I_\nu/N_H)^{ref}$).

ν (GHz)	$(I_\nu/N_H)^{ref}$ [MJy/sr/10^{20} H cm^{-2}]	Offset [MJy/sr]
IRAS		
2998	$(6.95 \pm 0.94) \times 10^{-1}$	$(7.36 \pm 0.03) \times 10^{-1}$
DIRBE:		
2998	$(6.60 \pm 0.01) \times 10^{-1}$	$(7.72 \pm 0.22) \times 10^{-1}$
2141	1.16 ± 0.01	1.41 ± 0.16
1249	$(8.85 \pm 0.04) \times 10^{-1}$	$(8.46 \pm 0.90) \times 10^{-1}$
Planck-HFI:		
857	$(5.43 \pm 0.38) \times 10^{-1}$	$(2.57 \pm 0.05) \times 10^{-1}$
545	$(1.82 \pm 0.13) \times 10^{-1}$	$(1.83 \pm 0.05) \times 10^{-1}$
353	$(4.84 \pm 0.10) \times 10^{-2}$	$(9.50 \pm 0.24) \times 10^{-2}$
217	$(1.14 \pm 0.03) \times 10^{-2}$	$(3.45 \pm 0.11) \times 10^{-2}$
143	$(2.92 \pm 0.07) \times 10^{-3}$	$(1.01 \pm 0.06) \times 10^{-2}$
100	$(1.13 \pm 0.04) \times 10^{-3}$	$(3.34 \pm 0.60) \times 10^{-3}$
Planck-LFI:		
70.3	$(8.74 \pm 2.66) \times 10^{-5}$	$(-6.40 \pm 0.93)\ 10^{-3}$
44.1	$(1.14 \pm 0.16) \times 10^{-4}$	$(-7.02 \pm 0.45)\ 10^{-3}$
28.5	$(2.11 \pm 0.14) \times 10^{-4}$	$(-6.95 \pm 0.15)\ 10^{-3}$
WMAP:		
93.7	$(-1.05 \pm 0.57) \times 10^{-4}$	$(-1.65 \pm 1.02) \times 10^{-3}$
61.2	$(-1.14 \pm 0.27) \times 10^{-4}$	$(-4.90 \pm 3.63) \times 10^{-4}$
41.1	$(3.52 \pm 1.13) \times 10^{-5}$	$(9.76 \pm 1.28) \times 10^{-4}$
32.9	$(1.39 \pm 0.08) \times 10^{-4}$	$(4.10 \pm 0.97) \times 10^{-4}$
23.1	$(2.69 \pm 0.04) \times 10^{-4}$	$(8.49 \pm 0.44) \times 10^{-4}$

Notes. Offsets derived from an empty region with $N_H^{HI} < 2.0 \times 10^{19}$ H cm^{-2}, assuming the same emissivity $(I_\nu/N_H)^{ref}$. The uncertainties are given at the 1σ level. The corresponding data are plotted in Fig. 2.

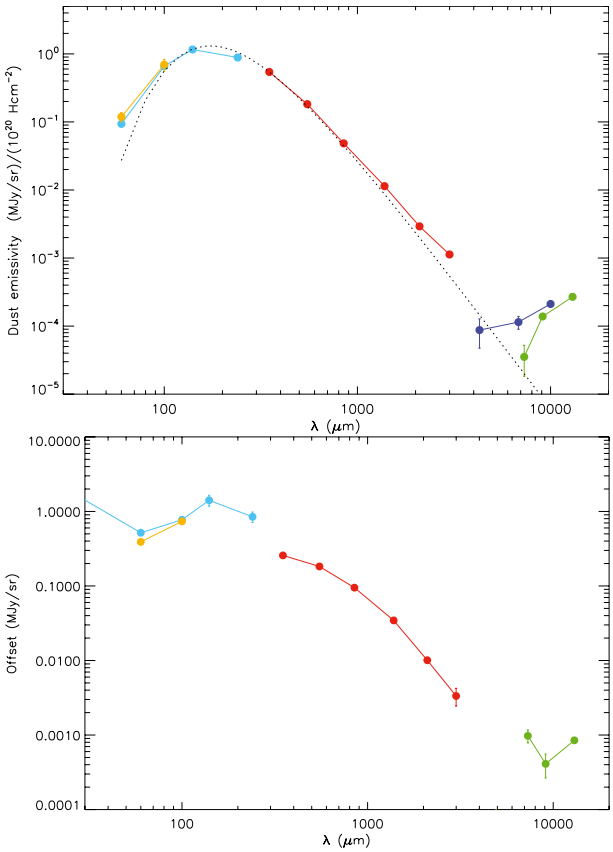

Fig. 2. *Upper panel*: thermal dust emissivity $(I_\nu/N_H)^{ref}$ from Table 2. The dot curve shows a modified black-body at $T_D = 17.5$ K and $\beta = 1.8$ normalized at 857 GHz, for comparison. The various colours are for different instruments: IRAS (Yellow), DIRBE (light blue), *Planck*-HFI (red), WMAP (dark blue) and *Planck*-LFI (green). *Lower panel*: Offsets from Table 2. The error bars are plotted at $\pm 3\sigma$.

3. Dust temperature and emissivity

3.1. Temperature determination

As shown in previous studies (e.g. Reach et al. 1995; Finkbeiner et al. 1999; Paradis et al. 2009; Planck Collaboration 2011t,u), the dust emissivity spectrum in our Galaxy cannot be represented by a single dust emissivity index β over the full FIR-submm domain. The data available indicate that β is usually steeper in the FIR and flatter in the submm band, with a transition around 500 μm. As dust temperature is best derived around the emission peak, we limit the range of frequencies used in the determination to the FIR, which limits the impact of a potential change of β with frequency.

In addition, the dust temperature derived will depend on the assumption made about β, since these two parameters are somewhat degenerate in χ^2 space. In order to minimize the above effect, we derived dust temperature maps using a fixed value of the dust emissivity index β. The selected β value was derived by fitting each pixel of the maps with a modified black body of the form $I_\nu \propto \nu^\beta B_\nu(T_D)$ in the above spectral range (method referred to as "free β"). This leads to a median value of $T_D = 17.7$ K and $\beta = 1.8$ in the region at $|b_{II}| > 10°$. Note that the β value is consistent with that derived from the combination of the FIRAS and *Planck*- HFI data at low column density in Planck Collaboration (2011t). Inspection of the corresponding T_D and β maps indeed showed spurious values of both parameters, caused by their correlation and the presence of noise in the data, in particular in low brightness regions of the maps.

We then performed fits to the FIR emission using the fixed $\beta = 1.8$ value derived above (method referred to as "fixed β"). In the determination of T_D, we used the IRIS 100 μm map and the two highest HFI frequencies at 857 and 545 GHz. Although the median reduced χ^2 is slightly higher than for the "free β" method, the temperature maps show fewer spurious values, in particular in low brightness regions. This results in a sharper distribution of the temperature histogram. Since we later use the temperature maps to investigate the spectral distribution of the dust optical depth and the dust temperature is a source of uncertainty, we adopt the "fixed β" method maps in the following. The corresponding temperature and uncertainty maps are shown in Fig. 3.

Temperature maps were derived at the common resolution of those three channels as well as at the resolution of lower intensity data. The model was used to compute emission in each photometric channels of the instruments used here (IRAS, *Planck*-HFI), taking into account the colour corrections using the actual transmission profiles for each instrument and following the adopted flux convention. In the interest of computing efficiency, the predictions of a given model were tabulated for a large set of parameters (T_D, β). For each map pixel, the χ^2 was computed

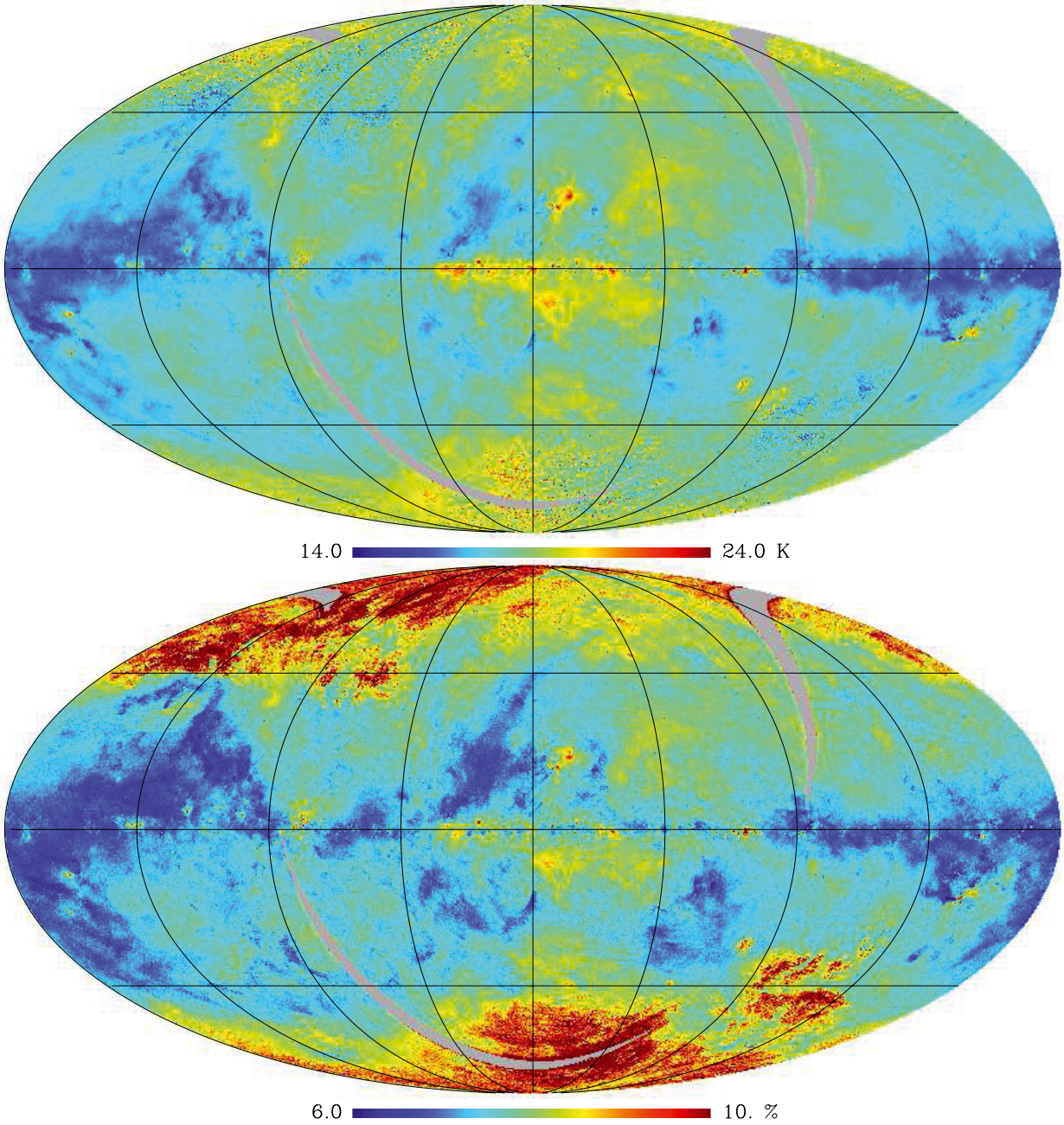

Fig. 3. *Upper panel*: all sky map of the dust temperature in K. The temperature is derived from modeling the IRIS 100 μm and the *Planck*-HFI emission at 857 and 545 GHz. *Lower panel*: all sky map of the dust temperature uncertainty in %. The maps are shown in Galactic coordinates with the Galactic centre at the centre of the image. Grey regions correspond to missing IRAS data.

for each entry of the table and the shape of the χ^2 distribution around the minimum value was used to derive the uncertainty on the free parameters. This included the effect of the data variance $\sigma^2_{\rm II}$ and the absolute uncertainties.

3.2. Angular distribution of dust temperature

The all-sky map of the thermal dust temperature computed as described in Sect. 3.1 for $\beta = 1.8$ is shown in Fig. 3. The elongated regions with missing values in the map correspond to the IRAS gaps, where the temperature cannot be determined from the *Planck*-HFI data alone. The distribution of the temperature clearly reflects the large scale distribution of the VIS-UV starlight radiation field intensity.

Along the Galactic plane, a large gradient can be seen from the outer Galactic regions, with $T_{\rm D} \simeq 14{-}15$ K to the inner Galactic regions around the Galactic center regions with $T_{\rm D} \simeq 19$ K. This asymmetry was already seen at lower angular resolution in the DIRBE (Sodroski et al. 1994) and the FIRAS (Reach et al. 1995) data. The asymmetry is probably due to the presence of more massive stars in the inner Milky Way regions, in particular in the molecular ring. The presence of warmer dust in the inner Galaxy is actually clearly highlighted by the radial distribution of the dust temperature derived from Galactic inversion of IR data (e.g. Sodroski et al. 1994; Paladini et al. 2007; Planck Collaboration 2011q). The origin of the large scale region near $(l_{\rm II}, b_{\rm II}) = (340°, -10°)$ with $T_{\rm D} \simeq 20$ K is currently unclear, but we note that it corresponds to a region of enhanced X-ray emission in the Rosat All-Sky Survey (RASS).

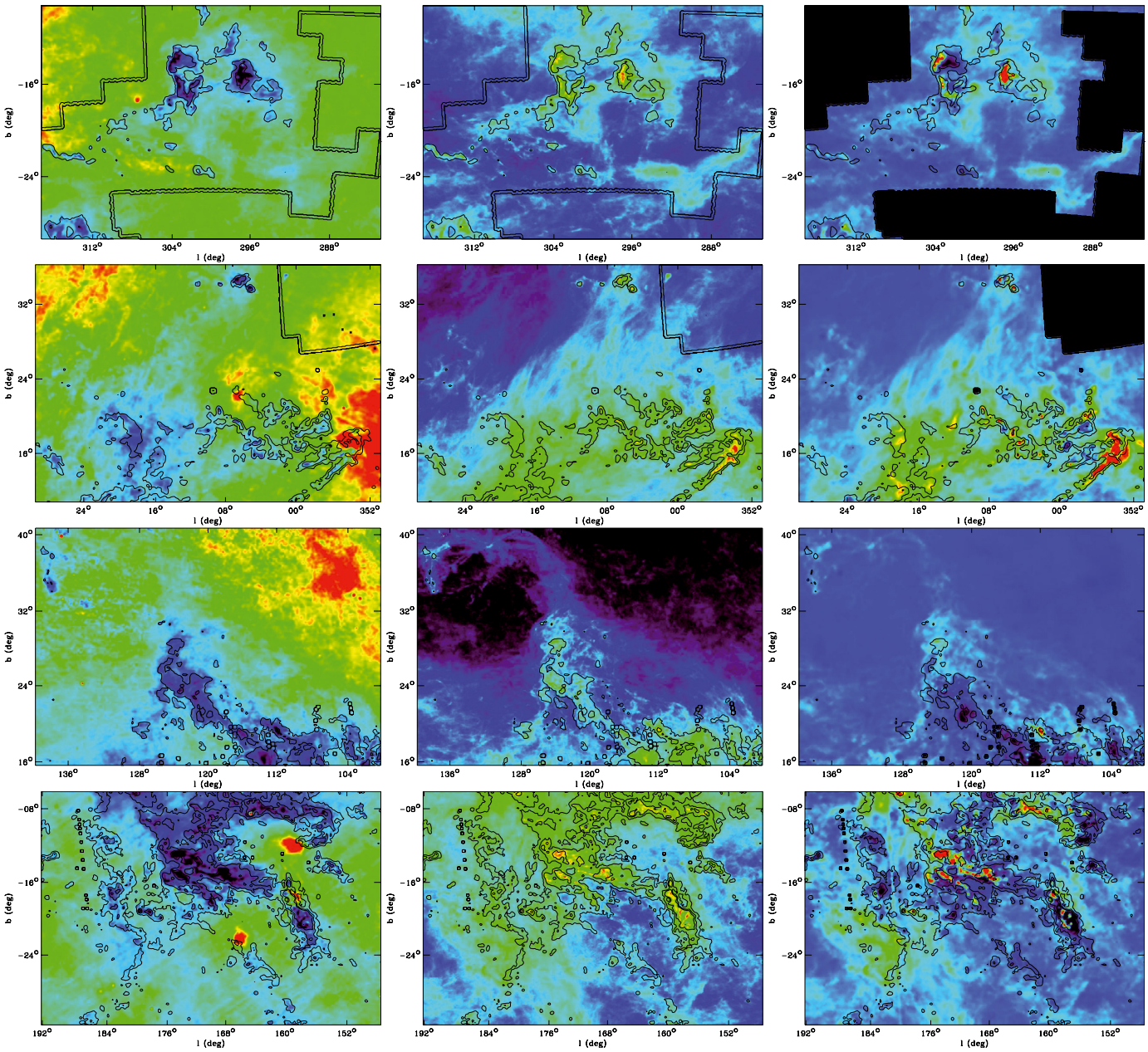

Fig. 4. Details of the dust temperature (*left column*), dust optical depth at 857 GHz (*central column*) and dark gas column density (*right column*) for the Chamaeleon (first line), Aquila-Ophiuchus flare (second line), Polaris flare (third line) and Taurus (fourth line). The temperature and optical depth maps are shown in log scale with a colour scale ranging from 15 K (black) to 20 K (red) and 1×10^{-5} (black) to 3×10^{-3} (red) respectively. The dark gas column density derived from the optical depth at 857 GHz (see Sect. 4) and is shown in linear scale with a colour scale ranging from –3 (black) to 7×10^{21} H cm^{-2} (red). The contours show the ^{12}CO($J = 1 \rightarrow 0$) integrated intensity at 2, 10 and 20 K km s^{-1}. The double line shows the limit of the CO surveys.

It may therefore correspond to warm dust associated with hot gas pervading the local bubble around the Sun, or a pocket of hot gas in Loop I. Similar large regions with enhanced dust temperature, such as near ($l_{\rm II}$, $b_{\rm II}$) = (340°, −30°) or ($l_{\rm II}$, $b_{\rm II}$) = (315°, +30°) may have a similar origin. Loop I ($l_{\rm II}$, $b_{\rm II}$) = (30°, +45°) is seen as a slightly warmer than average structure at $T_{\rm D} \simeq 19$ K. Running parallel to it is the Aquila-Ophiuchus flare ($l_{\rm II}$,$b_{\rm II}$) = (30°, +20°) with apparent $T_{\rm D} \simeq 14$ K extending to latitudes as high as 60°. The Cepheus and Polaris Flare ($l_{\rm II}$, $b_{\rm II}$) = (100–120°, +10–+20°) (see Planck Collaboration 2011t, for a detailed study) is also clearly visible as a lower temperature arch extending up to $b_{\rm II} = 30°$ into the North Celestial Pole loop and containing a collection of even colder condensations ($T_{\rm D} \simeq 12$–13 K).

On small angular scales, which are accessible over the whole sky only with the combination of the IRAS and *Planck*- HFI data at 5′, the map shows a variety of structures that can all be identified with local heating by known single stars or H II regions for warmer spots and with molecular clouds for colder regions. Figure 4 illustrates the high resolution spatial distribution of dust temperature and dust optical depth around some of these regions. Warmer regions include the tangent directions to the spiral Galactic arms in Cygnus ($l_{\rm II}$, $b_{\rm II}$) = (80°, 0°) and Carina ($l_{\rm II}$, $b_{\rm II}$) = (280°, 0°), hosts to many OB associations, and many H II regions along the plane. At higher Galactic latitude, dust heated by individual hot stars such in the Ophiuchi region ($l_{\rm II}$, $b_{\rm II}$) = (340°, +20°) with individual stars σ − Sco, ν − Sco,

ρ − Oph, ζ − Oph, in Orion ($l_{\rm II}$, $b_{\rm II}$) = (210°, −20°) with the Trapezium stars or in Perseus-Taurus ($l_{\rm II}$, $b_{\rm II}$) = (160°, −20°) with the California Nebula (NGC1499) can clearly be identified. Note the Spica HII region at ($l_{\rm II}$, $b_{\rm II}$) = (300°, +50°) where dust temperatures are $T_{\rm D} \simeq 20$ K due to heating by UV photons from the nearby (80 pc) early-type, giant (B1III) star α Vir.

At intermediate and high latitudes, nearby molecular clouds generally stand out as cold dust environments with $T_{\rm D} \simeq 13$ K. The most noticeable ones are Taurus ($l_{\rm II}$,$b_{\rm II}$)=(160°,−20°) (see Planck Collaboration 2011u, for a detailed study), RCrA ($l_{\rm II}$, $b_{\rm II}$) = (0°, −25°), Chamaeleon ($l_{\rm II}$, $b_{\rm II}$) = (300°, −20°) and Orion ($l_{\rm II}$, $b_{\rm II}$) = (200°, −20°). Numerous cold small scale condensations can readily be found when inspecting the temperature map, which mostly correspond to cold cores similar to those discovered at higher resolution in the *Herschel* data (e.g. André et al. 2010; Könyves et al. 2010; Molinari et al. 2010; Juvela et al. 2010) and in the *Planck* Cold-Core catalog (see Planck Collaboration 2011r,s).

Individual nearby Galaxies are also readily identified, in particular the Large ($l_{\rm II}$, $b_{\rm II}$) = (279°, −34°) and the Small Magellanic Cloud ($l_{\rm II}$, $b_{\rm II}$) = (301°, −44°) (see Planck Collaboration 2011m, for a detailed study), as well as M 31 and M 33.

Near the Galactic poles, the temperature determination becomes noisy at the 5′resolution due to the low signal levels.

3.3. Optical depth determination

Maps of the thermal dust optical depth ($\tau_{\rm D}(\lambda)$) are derived using:

$$\tau_{\rm D}(\lambda) = \frac{I_\nu(\lambda)}{B_\nu(T_{\rm D})}, \quad (2)$$

where B_ν is the Planck function and $I_\nu(\lambda)$ is the intensity map at frequency ν. The maps are shown in Fig. 5. We used resolution-matched maps of $T_{\rm D}$ and $I_\nu(\lambda)$ and derived $\tau_{\rm D}(\lambda)$ maps at the various resolutions of the data used here. The maps of the uncertainty on $\tau_{\rm D}(\lambda)$ ($\Delta\tau_{\rm D}$) are computed as:

$$\Delta\tau_{\rm D}(\nu) = \tau_{\rm D}\left(\frac{\sigma_{\rm II}^2}{I_\nu^2} + \left(\frac{\delta B_\nu}{\delta T}(T_{\rm D})\right)^2 \frac{\Delta T_{\rm D}^2}{B_\nu^2(T_{\rm D})}\right)^{1/2}. \quad (3)$$

4. Dust/gas correlation

We model the dust opacity ($\tau_{\rm M}$) as

$$\tau_{\rm M}(\lambda) = \left(\frac{\tau_{\rm D}(\lambda)}{N_{\rm H}}\right)^{\rm ref} [N_{\rm HI} + 2{\rm X_{CO}W_{CO}}], \quad (4)$$

where $\left(\frac{\tau_{\rm D}(\lambda)}{N_{\rm H}}\right)^{\rm ref}$ is the reference dust emissivity measured in low $N_{\rm H}$ regions and $X_{\rm CO} = N_{\rm H_2}/W_{\rm CO}$ is the traditional H_2/CO conversion factor. It is implicitly assumed that the dust opacity per unit gas column density is the same in the atomic and molecular gas. If this is not the case, this will directly impact our derived $X_{\rm CO}$ since only the product of $X_{\rm CO}$ by the dust emissivity in the CO phase $\left(\frac{\tau_{\rm D}}{N_{\rm H}}\right)^{\rm CO}$ can be derived here. The fit to derive the free parameters of the model is performed only in the portion of the sky covered by all surveys (infrared, H I, and CO) and where either (1) the extinction is less than a threshold $A_V^{\rm DG}$, or (2) the CO is detected with $W_{\rm CO} > 1$ K km s^{-1}. Criterion (1) selects the low-column density regions that are entirely atomic and suffer very small H I optical depth effects, so that the dust in this region will be associated with the H I emission at 21-cm. Criterion (2) selects regions where the CO is significantly detected and the dust is associated with both the H I and the ^{12}CO emission lines. We fit for the following three free parameters: $\left(\frac{\tau_{\rm D}}{N_{\rm H}}\right)^{\rm ref}$, $X_{\rm CO}$ and $A_V^{\rm DG}$. Note that, although $A_V^{\rm DG}$ does not enter Eq. (4) it is nonetheless derived from the fit since it enters the selection of the data points we use in the fit. The threshold $A_V^{\rm DG}$ measures the extinction (or equivalently the column density) where the correlation between the dust optical depth and the H I column density becomes non-linear.

The correlation between the optical depth for various photometric channels and the total gas column density ($N_{\rm H}^{\rm tot} = N_{\rm HI} + 2X_{\rm CO}W_{\rm CO}$) is shown in Fig. 6. The correlations were computed in the region of the sky where the CO data is available (about 63% of the sky) and at Galactic latitudes larger than $|b_{\rm II}| > 10°$. The $\tau_{\rm D}$ and $W_{\rm CO}$ maps used were smoothed to the common resolution of the H I map (0.6°). For these plots, we used a fixed value of $X_{\rm CO} = 2.3 \times 10^{20}$ H$_2$ cm^{-2}/(K km s^{-1}). The colours show the density of points in $N_{\rm H}^{\rm tot}$ and $\tau_{\rm D}$ bins. The dots show the $N_{\rm H}^{\rm tot}$ binned average correlation. The larger scatter of these points at high $N_{\rm H}^{\rm tot}$ comes from the limited number of points in the corresponding bins. The red line shows the $\tau_{\rm M}$ model values derived from the fit (slope = $\left(\frac{\tau_{\rm D}}{N_{\rm H}}\right)^{\rm ref}$) to the low $N_{\rm H}^{\rm tot}$ part of the data.

It can be seen that the correlation is linear at low $N_{\rm H}^{\rm tot}$ values and then departs from linear at $N_{\rm H}^{\rm tot} \simeq 8.0 \times 10^{20}$ H cm^{-2} ($A_V^{\rm DG} \simeq 0.4$ mag). Above $N_{\rm H}^{\rm tot} \simeq 5 \times 10^{21}$ H cm^{-2} ($A_v^{\rm H_2/CO} \simeq 2.5$ mag), where $N_{\rm H}^{\rm tot}$ becomes dominated by the CO contribution, the dust optical depth again is consistent with the observed correlation at low $N_{\rm H}^{\rm tot}$ for this given choice of the $X_{\rm CO}$ value. Between these two limits, the dust optical depth is in excess of the linear correlation. The same trend is observed in all photometric channels shown, with a similar value for the threshold. It is also observed in the HFI bands at lower frequencies, but the increasing noise at low $N_{\rm H}^{\rm tot}$ prevents an accurate determination of the fit parameters.

The best fit parameters for $\left(\frac{\tau_{\rm D}}{N_{\rm H}}\right)^{\rm ref}$, $X_{\rm CO}$ and $A_V^{\rm DG}$ are given in Table 3. They were derived separately for each frequency. The uncertainty was derived from the analysis of the fitted χ^2 around the best value. The $\left(\frac{\tau_{\rm D}}{N_{\rm H}}\right)^{\rm ref}$ values decrease with increasing wavelength, as expected for dust emission. The resulting dust optical depth SED is shown in Fig. 7. The dust optical depth in low column density regions is compatible with $\beta = 1.8$ at high frequencies. The best fit β value between the IRAS 100 μm and the HFI 857 GHz_is actually found to be $\beta = 1.75$. The SED then flattens slightly at intermediate frequencies with a slope of $\beta = 1.57$ around $\lambda = 500\,\mu$m then steepens again to $\beta = 1.75$ above 1 mm. The $X_{\rm CO}$ values derived from the fit are constant within the error bars, which increase with wavelength. The average value, computed using a weight proportional to the inverse variance is given in Table 3 and is found to be $X_{\rm CO} = 2.54 \pm 0.13 \times 10^{20}$ H$_2$ cm^{-2}/(K km s^{-1}). Similarly, the $A_V^{\rm DG}$ parameter does not significantly change over the whole frequency range and the weighted average value is found to be $A_V^{\rm DG} = 0.4 \pm 0.029$ mag.

The excess column density is defined using the difference between the best fit and the observed dust opacity per unit column density using,

$$N_{\rm H}^{\rm x} \equiv (\tau_{\rm D} - \tau_{\rm M})/\left(\frac{\tau_{\rm D}}{N_{\rm H}}\right)^{\rm ref}. \quad (5)$$

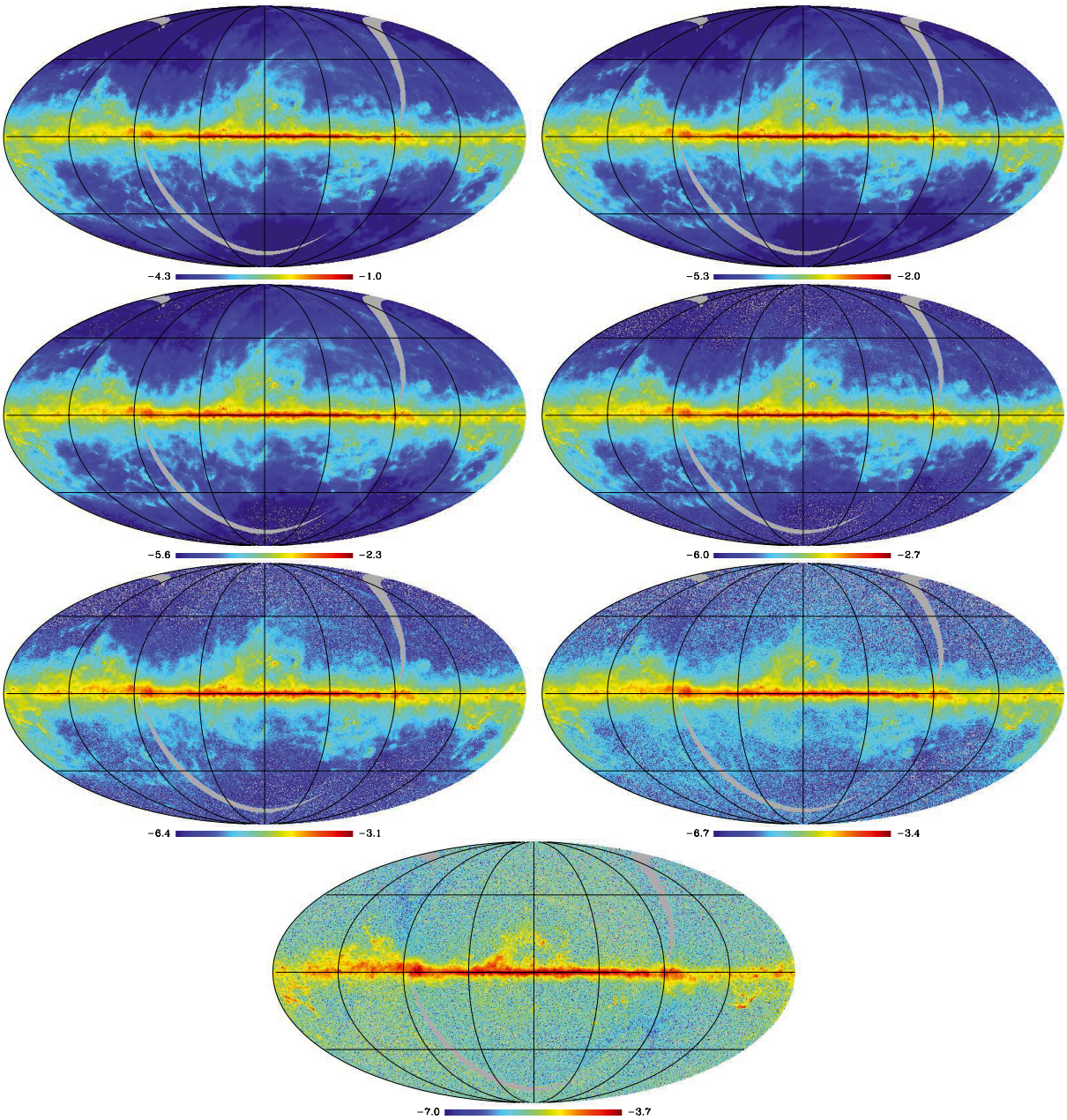

Fig. 5. Maps of the dust optical depths on a log scale, in the IRAS 100 μm (*first row left*) and *Planck*- HFI bands at 857 (*first row right*), 545 (*second row left*), 353 (*second row right*), 217 (*third row left*), 143 (*third row right*) and 100 GHz (*fourth row*). All maps are shown in Galactic coordinates with the Galactic centre at the centre of the image. The missing data in all images correspond to the IRAS gaps. The upper and lower bounds of the colour scale are set to $\tau_{\rm min} = 5 \times 10^{-5} \times (\lambda/100\,\mu{\rm m})^{-1.8}$ and $\tau_{\rm max} = 10^{-2} \times (\lambda/100\,\mu{\rm m})^{-1.8}$ respectively.

Table 3. Derived parameters for the dark gas, computed in the region with available CO data and $|b_{\rm II}| > 10°$.

Frequency [GHz]	$\tau_{\rm D}/N_{\rm H}^{\rm obs}$ [10^{-25} cm^2]	$X_{\rm CO}$ [H$_2$ cm^{-2}/(K km s^{-1})]	$A_V^{\rm DG}$ [mag]	$M_{\rm H}^X/M_{\rm H}^{\rm HI}$ –	$M_{\rm H}^X/M_{\rm H}^{\rm CO}$ –
2998	4.66 ± 0.65	$(2.60 \pm 0.18) \times 10^{20}$	$(4.05 \pm 0.39) \times 10^{-1}$	$(2.91 \pm 0.38) \times 10^{-1}$	1.27 ± 0.16
857	$(5.25 \pm 0.49) \times 10^{-1}$	$(2.52 \pm 0.29) \times 10^{20}$	$(3.92 \pm 0.64) \times 10^{-1}$	$(2.73 \pm 0.66) \times 10^{-1}$	1.22 ± 0.30
545	$(2.53 \pm 0.29) \times 10^{-1}$	$(2.52 \pm 0.36) \times 10^{20}$	$(3.96 \pm 0.79) \times 10^{-1}$	$(2.77 \pm 0.95) \times 10^{-1}$	1.24 ± 0.43
353	$(1.18 \pm 0.17) \times 10^{-1}$	$(2.31 \pm 0.47) \times 10^{20}$	$(4.07 \pm 1.28) \times 10^{-1}$	$(2.26 \pm 0.67) \times 10^{-1}$	1.10 ± 0.33
217	$(6.03 \pm 1.19) \times 10^{-2}$	$(2.58 \pm 0.67) \times 10^{20}$	$(4.60 \pm 2.39) \times 10^{-1}$	$(1.71 \pm 4.60) \times 10^{-1}$	$(7.46 \pm 20.09) \times 10^{-1}$
143	$(2.98 \pm 1.15) \times 10^{-2}$	$(1.83 \pm 1.00) \times 10^{20}$	$(4.62 \pm 4.81) \times 10^{-1}$	–	–
100	$(2.08 \pm 0.48) \times 10^{-2}$	$(4.05 \pm 1.93) \times 10^{20}$	$(6.69 \pm 5.15) \times 10^{-1}$	–	–
Average	–	$(2.54 \pm 0.13) \times 10^{20}$	$(4.03 \pm 0.29) \times 10^{-1}$	$(2.78 \pm 0.28) \times 10^{-1}$	1.18 ± 0.12

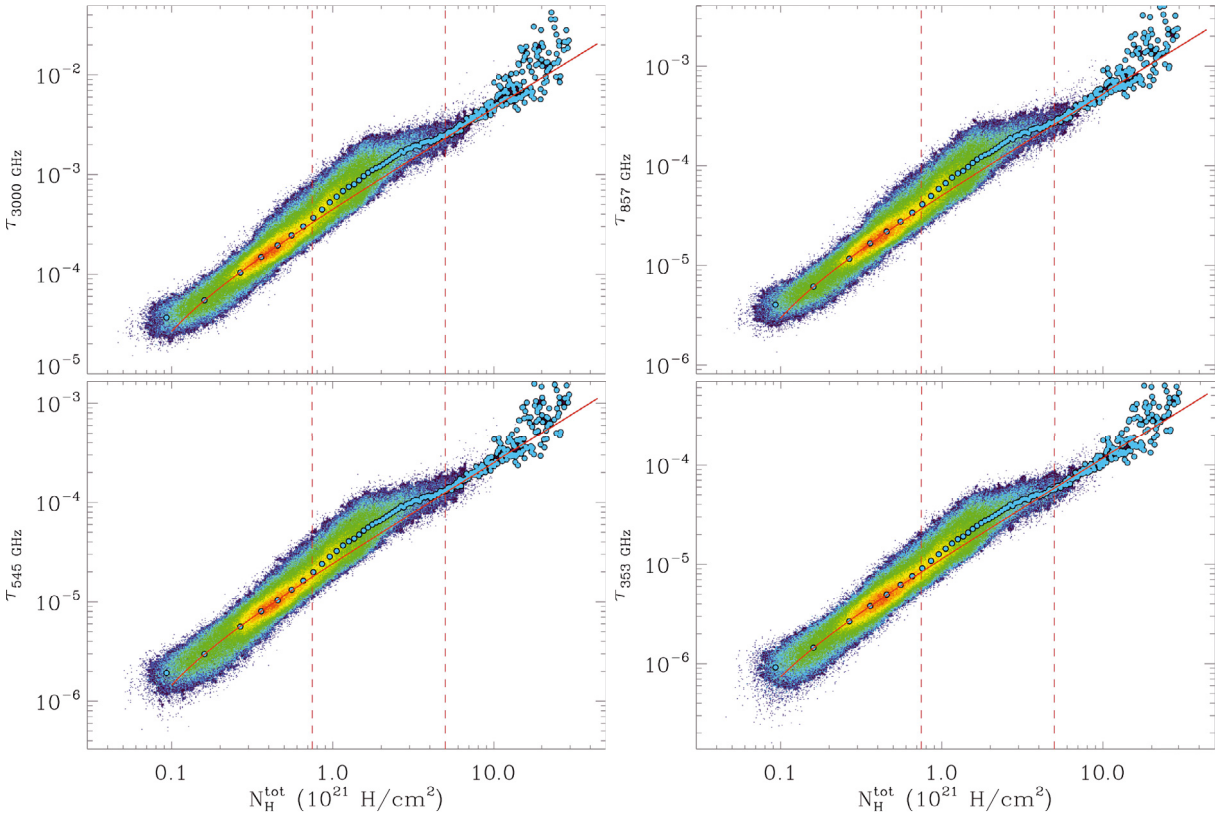

Fig. 6. Correlation plots between the dust optical depth at IRAS 100 μm (*upper left*), HFI 857 GHz (*upper right*), 545 GHz (*lower left*) and 353 GHz (*lower right*) and the total gas column density $N_{\rm H}^{\rm obs}$ in the solar neighbourhood ($|b_{\rm II}| > 10°$). The color scale represents the density of sky pixels on a log scale. The blue dots show a $N_{\rm H}^{\rm obs}$-binned average representation of the correlation. The red line shows the best linear correlation derived at low $N_{\rm H}^{\rm obs}$ values ($\tau = \left(\frac{\tau_{\rm D}}{N_{\rm H}}\right)^{\rm ref} * N_{\rm H}^{\rm obs} + \tau_0$). The vertical lines show the positions corresponding to $A_{\rm V} = 0.37$ mag and $A_{\rm V} = 2.5$ mag. These figures are shown for a single $X_{\rm CO} = 2.3 \times 10^{20}\,{\rm H_2\,cm^{-2}/(K\,km\,s^{-1})}$.

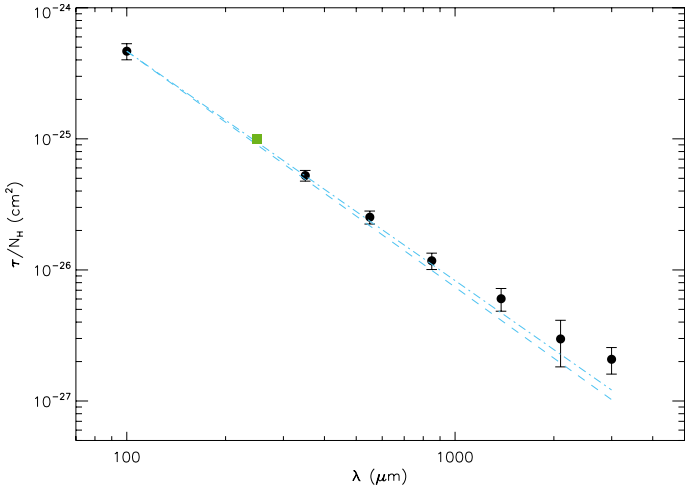

Fig. 7. Dust optical depth derived from this study using the IRAS and *Planck*- HFI frequencies. The square symbol shows the emissivity at 250 μm derived by Boulanger et al. (1996). The dash and dash-dot lines show a power law emissivity with $\lambda^{-1.8}$ and $\lambda^{-1.75}$ respectively, normalized to the data at 100 μm. The error bars shown are $\pm 1\sigma$.

The $N_{\rm H}^{\rm x}$ map is used to derive the total excess mass ($M_{\rm H}^{\rm x}$) assuming a fiducial distance of 200 pc to the gas responsible for the excess.

We also computed the atomic and molecular total gas masses over the same region of the sky, assuming the atomic and molecular gas emissions arise from a gas volume at the same distance. In the region covered by the CO survey, the H I to CO mass ratio derived for $X_{\rm CO} = 2.54 \times 10^{20}\,{\rm H_2\,cm^{-2}/(K\,km\,s^{-1})}$ is $M_{\rm HI}/M_{\rm CO} = 4$. Using the average $\left(\frac{\tau_{\rm D}}{N_{\rm H}}\right)^{\rm ref}$ and $X_{\rm CO}$ values above, the ratio of the dark gas mass to the atomic gas mass ($M_{\rm H}^x/M_{\rm H}^{\rm HI}$) and to the molecular gas mass ($M_{\rm H}^x/M_{\rm H}^{\rm CO}$) are given in Table 3. On average, at high Galactic latitudes, the dark gas masses are of the order of $28\% \pm 3\%$ of the atomic gas mass and $\simeq 118\% \pm 12\%$ of the molecular mass. We note that, since the scale-height of the HI layer is larger than that of the molecular layer, and that the dark gas component is likely to have an intermediate scale-height, the true $M_{\rm H}^x/M_{\rm H}^{\rm HI}$ and $M_{\rm H}^x/M_{\rm H}^{\rm CO}$ values are likely to be respectively lower and larger than the values quoted above, which assume the same distance for all three components.

5. Dark-gas spatial distribution

The spatial distribution of the dark gas as derived from $\tau_{\rm D}$ computed from the HFI 857 GHz channel is shown in Fig. 8. It is shown in the region where the CO data are available and above Galactic latitudes of $|b_{\rm II}| > 5°$. Regions where $W_{\rm CO} > 1\,{\rm K\,km\,s^{-1}}$ have also been excluded. The map clearly shows that the dark gas is distributed mainly around the best known molecular clouds such as Taurus, the Cepheus and Polaris flares, Chamaeleon and Orion. The strongest excess region is in the Aquila-Ophiuchus flare, which was already evident in Grenier et al. (2005).

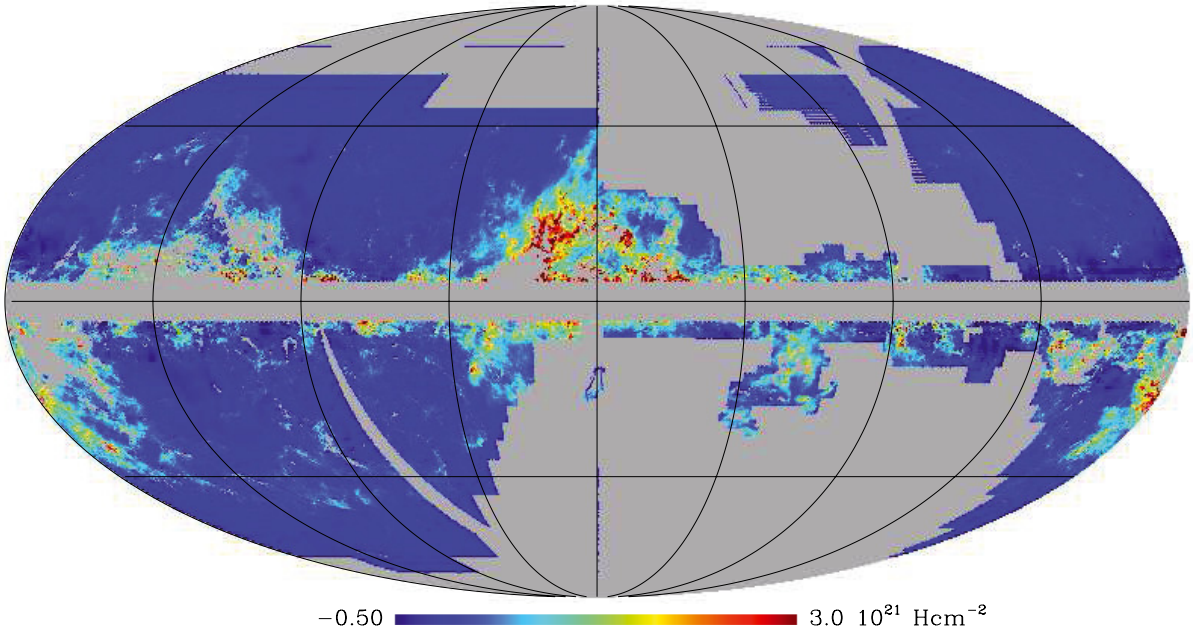

Fig. 8. Map of the excess column density derived from the 857 GHz data. The map is shown in Galactic coordinates with the Galactic centre at the centre of the image. The grey regions correspond to those where no IRAS or CO data are available, regions with intense CO emission ($W_{CO} > 1\,K\,km\,s^{-1}$) and the Galactic plane ($|b_{II}| < 5°$).

Significant dark gas is also apparent at high latitudes, south of the Galactic plane in the anticenter and around known translucent molecular clouds, such as MBM53 ($l_{II} = 90°$, $b_{II} = -30°$). As with all the molecular clouds, the spatial distribution of the dark gas closely follows that of the Gould-Belt (Perrot & Grenier 2003) and indicates that most of the dark gas in the solar neighbourhood belongs to this dynamical structure.

6. Discussion

6.1. Dust emissivity in the atomic neutral gas

In the solar neighbourhood, Boulanger et al. (1996) measured an emissivity value in the diffuse medium of $10^{-25}\,cm^2/H$ at 250 μm assuming a spectral index $\beta = 2$ which seemed consistent with their data. The optical depth of dust derived in our study in the low N_H^{tot} regions at $|b_{II}| > 10°$ is shown in Fig. 7. The figure also shows the reference value by Boulanger et al. (1996) which is in good agreement with the values derived here, interpolated at 250 μm (in fact 10% above when using $\beta = 1.8$ and 6% above when using $\beta = 1.75$). Our study does not allow us to measure the emissivity in the molecular gas, since we are only sensitive to the product of this emissivity with the X_{CO} factor. However, we note that our derived average $X_{CO} = 2.54 \times 10^{20}\,H_2\,cm^{-2}/(K\,km\,s^{-1})$ is significantly higher than previously derived values. Even if we account for the possible uncertainty in the calibration of the $^{12}CO(J = 1 \rightarrow 0)$ emission (24%) discussed in Sect. 2.2.2, increasing the CO emission by the corresponding factor would only lower our X_{CO} estimate to $X_{CO} = 2.2\,H_2\,cm^{-2}/(K\,km\,s^{-1})$. In comparison, a value of $(1.8 \pm 0.3) \times 10^{20}\,H_2\,cm^{-2}/(K\,km\,s^{-1})$ was found at $|b_{II}| > 5°$ from the comparison of the H I, CO, and IRAS 100 μm maps (Dame et al. 2001). Similarly, values derived from γ-ray *Fermi* data can be as low as $X_{CO} = 0.87 \times 10^{20}\,H_2\,cm^{-2}/(K\,km\,s^{-1})$ in Cepheus, Cassiopea and Polaris (Abdo et al. 2010). This could be evidence that the dust emissivity in the high-latitude molecular material could be larger than in the atomic phase by a factor ≃3. Such an increase in the dust emissivity in molecular regions has been inferred in previous studies (e.g. Bernard et al. 1999; Stepnik et al. 2003) and was attributed to dust aggregation.

6.2. Dark molecular gas

The nature of "dark molecular gas" has recently been investigated theoretically by Wolfire et al. (2010), who specifically address the HI/H_2 and C/C^+ transition at the edges of molecular clouds. The nominal cloud modeled in their study is relatively large, with total column density $1.5 \times 10^{22}\,cm^{-2}$, so the applicability of the results to the more translucent conditions of high-Galactic-latitude clouds is not guaranteed. The envelope of the cloud has an H I column density of $1.9 \times 10^{21}\,cm^{-2}$ which is more typical of the entire column density measured at high latitudes. Wolfire et al. (2010) define f_{DG} as the fraction of molecular gas that is dark, i.e. not detected by CO. In the nominal model, the chemical and photodissociation balance yields a total H_2 column density of $7.0 \times 10^{21}\,cm^{-2}$, while the "dark" H_2 in the transition region where CO is dissociated has a column density of $1.9 \times 10^{21}\,cm^{-2}$. The fraction of the total gas column density that is molecular,

$$f(H_2) = \frac{2N(H_2)}{2N(H_2) + N(HI)} \quad (6)$$

is 93% in the nominal model, which suggests that the line of sight through such a cloud passes through material which is almost entirely molecular. To compare the theoretical model to our observational results, we must put them into the same units. We define the dark gas fraction as the fraction of the total gas column density that is dark,

$$f_{DARK} = \frac{2N(H_2^{dark})}{2N(H_2) + N(HI)} = f(H_2) f_{DG}. \quad (7)$$

For the nominal Wolfire et al. (2010) model, $f_{DG} = 0.29$ so we can infer $f_{DARK} = 0.27$. The smaller clouds in Figure 11 of their paper have larger f_{DG}, but $f(H_2)$ is also probably smaller (not

given in the paper) so we cannot yet definitively match the model and observations. These model calculations are in general agreement with our observational results, in that a significant fraction of the molecular gas can be in CO-dissociated "dark" layers.

If we assume that all dark molecular gas in the solar neighbourhood is evenly distributed to the observed CO clouds, the average $f_{\rm DG}$ measured is in the range $f_{\rm DG} = 1.06-1.22$. This is more than three times larger than predicted by the Wolfire et al. (2010) mass fraction. This may indicate that molecular clouds less massive than the ones assumed in the model actually have a dark gas mass fraction higher by a factor of about three. This would contradict their conclusion that the dark mass fraction does not depend on the total cloud mass. We also note that Wolfire et al. (2010) used the Solomon et al. (1987) value for the mean column density of GMCs, but that a more recent study by Heyer et al. (2009) shows column density values 2–5 times lower. It can be expected that the reduced column density would allow deeper UV penetration and perhaps, a larger fractional composition of dark gas, as implied by our results.

The location of the H I-to-H_2 transition measured here ($A_V^{\rm DG} \simeq 0.4$ mag) is comparable, although slightly higher than that predicted in the Wolfire et al. (2010) model ($A_V^{\rm DG} \simeq 0.2$ mag). Again, this difference may indicate variations with the cloud size used, since UV shadowing by the cloud itself is expected to be less efficient for smaller clouds, leading to a transition deeper into the cloud.

Our results can also be compared with the amount of dark molecular gas inferred from recent observations of the CII transition with *Herschel* – HIFI in the framework of the GOT C+ survey (Langer et al. 2010). In transition clouds showing ^{12}CO emission but no ^{13}CO emission, Velusamy et al. (2010) found an average $M_{\rm H}^X/M_{\rm H}^{\rm CO} \simeq 0.41$, which is significantly smaller than our value of 1.18. This difference could be due to the different characteristics of the clouds included in the GOT C+ survey, which are more distant and probably of larger physical size than those studied here in the solar neighborhood. However, it is most likely that the differences are due to the CII emission sampling preferentially warm and dense regions of the ISM, owing to the density and temperature sensitivity of the excitation of the CII transition, while the dust based detection of the dark-gas described here is in principle sensitive to all densities. This difference would explain why we see larger dark gas fractions with respect to CO, because the CII observations are likely to miss part of the diffuse dark gas.

6.3. Other possible origins

The observed departure from linearity between $\tau_{\rm D}$ and the observable gas column density could also in principle be caused by variations of the dust/gas ratio (D/G). However, such variations with amplitude of 30% in the solar neighbourhood and a systematic trend for a higher D/G ratio in denser regions would be difficult to explain over such a small volume and in the presence of widespread enrichment by star formation. However, the fact that the dark gas is also seen in the γ-ray with comparable amplitudes is a strong indication that it originates from the gas phase. The dark gas column-densities inferred from the γ-ray observations are also consistent with a standard D/G ratio (Grenier et al. 2005).

The observed excess optical depth could also in principle be due to variations of the dust emissivity in the FIR-Submm. We expect such variations to occur if dust is in the form of aggregates with higher emissivity (e.g. Stepnik et al. 2003) in the dark gas region. We note however that such modifications of the optical properties mainly affect the FIR-submm emissivity and are not expected to modify significantly the absorption properties in the Visible. Therefore, detecting a similar departure from linearity between large-scale extinction maps and the observable gas would allow us to exclude this possibility.

Sky directions where no CO is detected at the sensitivity of the CO survey used (0.3–1.2 K km s^{-1}) may actually host significant CO emission, which could be responsible for the excess dust optical depth observed. Evidences for such diffuse and weakly emitting CO gas have been reported. For instance, in their study of the large-scale molecular emission of the Taurus complex, Goldsmith et al. (2008) have found that half the mass of the complex is in regions of low column density $N_{\rm H} < 2\times10^{21}$ cm^{-2}, seen below $W_{\rm CO} \simeq 1$ K km s^{-1}. However, Barriault et al. (2010) reported a poor spatial correlation between emission by diffuse CO and regions of FIR excess in two high Galactic latitude regions in the Polaris Flare and Ursa Major. The difficulty at finding the CO emission associated to dark gas is that the edges of molecular clouds tend to be highly structured spatially, which could explain why many attempts have been unsuccessful (see for instance Falgarone et al. 1991). In our case, it is possible to obtain an upper limit to the contribution of weak CO emission below the survey detection threshold, by assuming that pixels with undetected CO emission actually emit with $W_{\rm CO} = 0.5$ K km s^{-1}. This is the detection limit of the survey we use at $|b| > 10°$ so this should be considered an upper limit to the contribution of undetected diffuse CO emission. In that case, the dark gas mass is reduced by a factor lower than 20%. This indicates that, although diffuse weak CO emission could contribute a fraction of the observed excess emission, it cannot produce the bulk of it.

Finally, we recognize that the optically thin approximation used here for the H I emission may not fully account for the whole atomic gas present, even at high latitude. H I emission is subject to self absorption and $N_{\rm H}$ can be underestimated from applying too high a spin temperature ($T_{\rm s}$) while deriving column densities. $T_{\rm s}$ is likely to vary from place to place depending on the relative abundance of CNM clumps (with thermodynamical temperatures of 20–100 K) and WNM clouds (at several thousand K) in the telescope beam. The effective spin temperature of 250–400 K to be applied to correct for this blending and to retrieve the total column density from the H I spectra does not vary much in the Galaxy (Dickey et al. 2003, 2009). It indicates that most of the H I mass is in the warm phase and that the relative abundance of cold and warm H I is nearly constant across the Galaxy (outside of the inner molecular ring). The correlation between the *Fermi* γ-ray maps and the H I column densities derived for different spin temperatures also support an average (uniform) effective spin temperature >250 K on and off the plane (Ackermann et al. 2011). In order to test these effects, we performed the analysis described in this paper using a very low choice for the H I spin temperature. We adopted a value of $T_{\rm s} = 80$ K when the observed H I peak temperature is below 80 K and $T_{\rm s} = 1.1 \times T_{\rm peak}$ when above. Under this hypothesis, we obtained dark gas fractions which are about half of those given in Table 3 under the optically thin approximation. We consider this to indicate that significantly less than half of the detected dark gas could be dense, cold atomic gas. We further note that, under the optically thin H I hypothesis, the dark gas fraction appears very constant with Galactic latitude down to $|b_{\rm II}| \simeq 3°$ (see Sect. 6.4), while it varies more strongly using $T_{\rm s} = 80$ K. This does not support the interpretation that the bulk of the dust excess results from underestimated H I column densities.

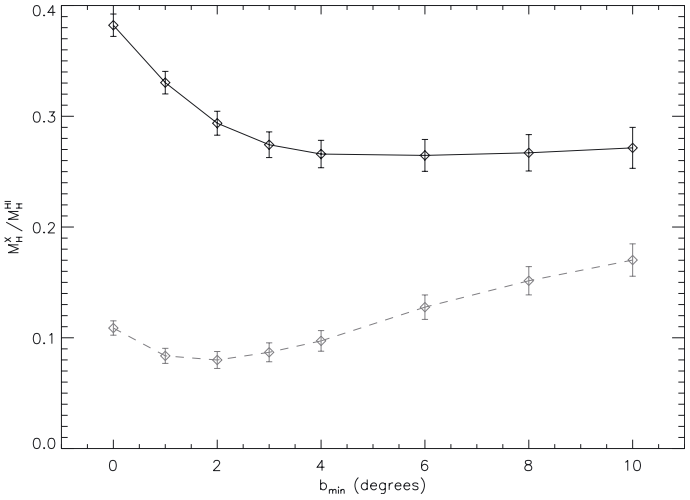

Fig. 9. Fractional mass of the dark gas with respect to the neutral gas mass as a function of the lower b_{II} value used in the analysis. The solid curve is computed under the assumption of optically thin H I, the dashed curve is for N_H^{HI} computed using $T_s = 80$ K. Error bars are 1σ.

6.4. Dark-gas variations with latitude

We investigate the distribution of the dark gas as a function of Galactic latitude. This is important, since the dark gas template produced here for the solar neighbourhood is also used in directions toward the plane for Galactic inversion purpose in Planck Collaboration (2011q). We performed the calculations described in Sect. 4 for various values of the Galactic latitude lower cutoff (b_{min}) in the range $b_{min} < |b_{II}| < 90°$ with b_{min} varying from 0° to 10°. For each value, we used the best fit parameters derived from $b_{min} = 10°$ and given in Table 3.

Figure 9 shows the evolution of the dark gas mass fraction with respect to the atomic gas mass as a function of b_{min}. It can be seen that the ratio changes only mildly (increases by a factor 1.12 from $b_{min} = 10°$ to $b_{min} = 2°$) as we approach the Galactic plane. This indicates that a fairly constant fraction of the dark gas derived from the solar neighbourhood can be applied to the rest of the Galaxy.

Figure 9 also shows the same quantity computed using the H I column density derived using $T_s = 80$ K. It can be seen that, in that case, the dark gas fraction is predicted to decrease by a factor 2.12 from $b_{min} = 10°$ to $b_{min} = 2°$. This is caused by the much larger inferred H I masses toward the plane under this hypothesis. We consider it unlikely that the dark gas fraction varies by such a large factor from the solar neighbourhood to the Galactic plane, and consider it more likely that the correction applied to N_H by using a spin temperature as low as $T_s = 80$ K actually strongly overestimates the H I opacity, and therefore the fraction of the dark gas belonging to atomic gas.

7. Conclusions

We used the *Planck*-HFI and IRAS data to determine all sky maps of the thermal dust temperature and optical depth. The temperature map traces the spatial variations of the radiation field intensity associated with star formation in the Galaxy. This type of map is very important for the detailed analysis of the dust properties and their spatial variations.

We examined the correlation between the dust optical depth and gas column density as derived from H I and CO observations. These two quantities are linearly correlated below a threshold column density of $N_H^{obs} < 8.0 \times 10^{20}$ H cm^{-2} corresponding to $A_V < 0.4$ mag. Below this threshold, we observed dust emissivities following a power-law with $\beta \simeq 1.8$ below $\lambda \simeq 500\,\mu$m and flattening at longer wavelengths. Absolute emissivity values derived in the FIR are consistent with previous estimates.

This linear correlation also holds at high column densities ($N_H^{obs} > 5 \times 10^{21}$ H cm^{-2}) corresponding to $A_V = 2.5$ mag where the total column density is dominated by the molecular phase for a given choice of the X_{CO} factor. Under the assumption that the dust emissivity is the same in both phases, this leads to an estimate of the average local CO to H_2 factor of $X_{CO} = 2.54 \times 10^{20}$ H$_2$ cm^{-2}/(K km s^{-1}). The optical depth in the intermediate column density range shows an excess in all photometric channels considered in this study. We interpret the excess as dust emission associated with dark gas, probably in the molecular phase where H_2 survives photodissociation, while the CO molecule does not.

In the solar neighbourhood, the derived mass of the dark gas, assuming the same dust emissivity as in the H I phase is found to correspond to ≃28% of the atomic mass and ≃118% of the molecular gas mass. The comparison of this value with the recent calculations for dark molecular gas around clouds more massive than the ones present in the solar neighbourhood indicates a dark gas fraction about three times larger in the solar neighbourhood. The threshold for the onset of the dark gas transition is found to be ≃0.4 mag and appears compatible to, although slightly larger than, the thresholds predicted by this model. Finally, we stress that the H I 21 cm line is unlikely to be fully optically thin and to measure all the atomic gas. Therefore, the dark gas detected here could well represent a mixture of dark molecular and dark (optically thick) atomic gas seen through its dust emission. For an average H I spin temperature of 80 K, the mixture is predicted to be 50% atomic and 50% molecular.

Acknowledgements. A description of the Planck Collaboration and a list of its members can be found at http://www.rssd.esa.int/index.php?project=PLANCK&page=Planck_Collaboration

References

Abdo, A. A., Ackermann, M., Ajello, M., et al. 2010, ApJ, 710, 133
Ackermann, M., Ajello, M., Baldini, L., et al. 2011, ApJ, 726, 81
André, P., Men'shchikov, A., Bontemps, S., et al. 2010, A&A, 518, L102
Arnal, E. M., Bajaja, E., Larrarte, J. J., Morras, R., & Pöppel, W. G. L. 2000, A&AS, 142, 35
Bajaja, E., Arnal, E. M., Larrarte, J. J., et al. 2005, A&A, 440, 767
Barriault, L., Joncas, G., Falgarone, E., et al. 2010, MNRAS, 406, 2713
Bernard, J., Reach, W. T., Paradis, D., et al. 2008, AJ, 136, 919
Bernard, J. P., Abergel, A., Ristorcelli, I., et al. 1999, A&A, 347, 640
Blitz, L., Bazell, D., & Desert, F. X. 1990, ApJ, 352, L13
Bohlin, R. C., Savage, B. D., & Drake, J. F. 1978, ApJ, 224, 132
Boulanger, F., Abergel, A., Bernard, J., et al. 1996, A&A, 312, 256
Dame, T. M. 2011, [arXiv:1101.1499]
Dame, T. M., Hartmann, D., & Thaddeus, P. 2001, ApJ, 547, 792
de Vries, H. W., Thaddeus, P., & Heithausen, A. 1987, ApJ, 319, 723
Dickey, J. M., McClure-Griffiths, N. M., Gaensler, B. M., & Green, A. J. 2003, ApJ, 585, 801
Dickey, J. M., Strasser, S., Gaensler, B. M., et al. 2009, ApJ, 693, 1250
Dickman, R. L., Snell, R. L., & Schloerb, F. P. 1986, ApJ, 309, 326
Falgarone, E., Phillips, T. G., & Walker, C. K. 1991, ApJ, 378, 186
Finkbeiner, D. P., Davis, M., & Schlegel, D. J. 1999, ApJ, 524, 867
Fukui, Y., Onishi, T., Abe, R., et al. 1999, PASJ, 51, 751
Gillmon, K., & Shull, J. M. 2006, ApJ, 636, 908
Glover, S. C. O., Federrath, C., Mac Low, M., & Klessen, R. S. 2010, MNRAS, 404, 2
Goldsmith, P. F., Heyer, M., Narayanan, G., et al. 2008, ApJ, 680, 428
Górski, K. M., Hivon, E., Banday, A. J., et al. 2005, ApJ, 622, 759
Grenier, I. A., Casandjian, J., & Terrier, R. 2005, Science, 307, 1292
Hartmann, D., & Burton, W. B. 1997, Atlas of Galactic Neutral Hydrogen, ed. D. Hartmann, & W. B. Burton

Hauser, M. G., Arendt, R. G., Kelsall, T., et al. 1998, ApJ, 508, 25
Heiles, C., Reach, W. T., & Koo, B. 1988, ApJ, 332, 313
Heyer, M., Krawczyk, C., Duval, J., & Jackson, J. M. 2009, ApJ, 699, 1092
Heyer, M. H., Carpenter, J. M., & Snell, R. L. 2001, ApJ, 551, 852
Juvela, M., Ristorcelli, I., Montier, L. A., et al. 2010, A&A, 518, L93
Kalberla, P. M. W., Burton, W. B., Hartmann, D., et al. 2005, A&A, 440, 775
Kawamura, A., Onishi, T., Mizuno, A., Ogawa, H., & Fukui, Y. 1999, PASJ, 51, 851
Könyves, V., André, P., Men'shchikov, A., et al. 2010, A&A, 518, L106
Kulkarni, S. R., & Heiles, C. 1988, in Galactic and extragalactic radio astronomy (Berlin, New York: Springer), 2nd edn, 95
Langer, W. D., Velusamy, T., Pineda, J. L., et al. 2010, A&A, 521, L17
Leroy, A., Bolatto, A., Stanimirovic, S., et al. 2007, ApJ, 658, 1027
Matsunaga, K., Mizuno, N., Moriguchi, Y., et al. 2001, PASJ, 53, 1003
Mennella, A., Butler, R. C., Curto, A., et al. 2011, A&A, 536, A3
Meyerdierks, H., & Heithausen, A. 1996, A&A, 313, 929
Miville-Deschênes, M., & Lagache, G. 2005, ApJS, 157, 302
Miville-Deschênes, M., Lagache, G., & Puget, J. 2002, A&A, 393, 749
Mizuno, A., & Fukui, Y. 2004, in Milky Way Surveys: The Structure and Evolution of our Galaxy, ed. D. Clemens, R. Shah, & T. Brainerd, ASP Conf. Ser., 317, 59
Mizuno, A., Yamaguchi, R., Tachihara, K., et al. 2001, PASJ, 53, 1071
Molinari, S., Swinyard, B., Bally, J., et al. 2010, A&A, 518, L100
Onishi, T., Kawamura, A., Abe, R., et al. 1999, PASJ, 51, 871
Onishi, T., Yoshikawa, N., Yamamoto, H., et al. 2001, PASJ, 53, 1017
Paladini, R., Montier, L., Giard, M., et al. 2007, A&A, 465, 839
Paradis, D., Bernard, J., & Mény, C. 2009, A&A, 506, 745
Perrot, C. A., & Grenier, I. A. 2003, A&A, 404, 519
Planck Collaboration 2011a, A&A, 536, A1
Planck Collaboration 2011b, A&A, 536, A2
Planck Collaboration 2011c, A&A, 536, A7
Planck Collaboration 2011d, A&A, 536, A8
Planck Collaboration 2011e, A&A, Vol., A9
Planck Collaboration 2011f, A&A, 536, A10
Planck Collaboration 2011g, A&A, 536, A11
Planck Collaboration 2011h, A&A, 536, A12
Planck Collaboration 2011i, A&A, 536, A13
Planck Collaboration 2011j, A&A, 536, A14
Planck Collaboration 2011k, A&A, 536, A15
Planck Collaboration 2011l, A&A, 536, A16
Planck Collaboration 2011m, A&A, 536, A17
Planck Collaboration 2011n, A&A, 536, A18
Planck Collaboration 2011o, A&A, 536, A19
Planck Collaboration 2011p, A&A, 536, A20
Planck Collaboration 2011q, A&A, 536, A21
Planck Collaboration 2011r, A&A, 536, A22
Planck Collaboration 2011s, A&A, 536, A23
Planck Collaboration 2011t, A&A, 536, A24
Planck Collaboration 2011u, A&A, 536, A25
Planck Collaboration 2011v, The Explanatory Supplement to the Planck Early Release Compact Source Catalogue (ESA)
Planck Collaboration 2011w, A&A, 536, A26
Planck HFI Core Team 2011a, A&A, 536, A4
Planck HFI Core Team 2011b, A&A, 536, A6
Reach, W. T., Koo, B., & Heiles, C. 1994, ApJ, 429, 672
Reach, W. T., Dwek, E., Fixsen, D. J., et al. 1995, ApJ, 451, 188
Reach, W. T., Wall, W. F., & Odegard, N. 1998, ApJ, 507, 507
Roman-Duval, J., Israel, F. P., Bolatto, A., et al. 2010, A&A, 518, L74
Savage, B. D., Bohlin, R. C., Drake, J. F., & Budich, W. 1977, ApJ, 216, 291
Sodroski, T. J., Bennett, C., Boggess, N., et al. 1994, ApJ, 428, 638
Solomon, P. M., Rivolo, A. R., Barrett, J., & Yahil, A. 1987, ApJ, 319, 730
Stepnik, B., Abergel, A., Bernard, J., et al. 2003, A&A, 398, 551
Velusamy, T., Langer, W. D., Pineda, J. L., et al. 2010, A&A, 521, L18
Wakker, B. P. 2006, ApJS, 163, 282
Wolfire, M. G., Hollenbach, D., & McKee, C. F. 2010, ApJ, 716, 1191
Zacchei, A., Maino, D., Baccigalupi, C., et al. 2011, A&A, 536, A5

[1] Aalto University Metsähovi Radio Observatory, Metsähovintie 114, 02540 Kylmälä, Finland
[2] Agenzia Spaziale Italiana Science Data Center, c/o ESRIN, via Galileo Galilei, Frascati, Italy
[3] Astroparticule et Cosmologie, CNRS (UMR7164), Université Denis Diderot Paris 7, Bâtiment Condorcet, 10 rue A. Domon et Léonie Duquet, Paris, France
[4] Astrophysics Group, Cavendish Laboratory, University of Cambridge, J J Thomson Avenue, Cambridge CB3 0HE, UK
[5] Atacama Large Millimeter/submillimeter Array, ALMA Santiago Central Offices, Alonso de Cordova 3107, Vitacura, Casilla 763 0355, Santiago, Chile
[6] CITA, University of Toronto, 60 St. George St., Toronto, ON M5S 3H8, Canada
[7] CNRS, IRAP, 9 Av. colonel Roche, BP 44346, 31028 Toulouse Cedex 4, France
[8] California Institute of Technology, Pasadena, California, USA
[9] Centre of Mathematics for Applications, University of Oslo, Blindern, Oslo, Norway
[10] DAMTP, University of Cambridge, Centre for Mathematical Sciences, Wilberforce Road, Cambridge CB3 0WA, UK
[11] DSM/Irfu/SPP, CEA-Saclay, 91191 Gif-sur-Yvette Cedex, France
[12] DTU Space, National Space Institute, Juliane Mariesvej 30, Copenhagen, Denmark
[13] Departamento de Física, Universidad de Oviedo, Avda. Calvo Sotelo s/n, Oviedo, Spain
[14] Department of Astronomy and Astrophysics, University of Toronto, 50 Saint George Street, Toronto, Ontario, Canada
[15] Department of Astronomy and Earth Sciences, Tokyo Gakugei University, Koganei, Tokyo 184-8501, Japan
[16] Department of Physical Science, Graduate School of Science, Osaka Prefecture University, 1-1 Gakuen-cho, Naka-ku, Sakai, Osaka 599-8531, Japan
[17] Department of Physics & Astronomy, University of British Columbia, 6224 Agricultural Road, Vancouver, British Columbia, Canada
[18] Department of Physics, Gustaf Hällströmin katu 2a, University of Helsinki, Helsinki, Finland
[19] Department of Physics, Nagoya University, Chikusa-ku, Nagoya, 464-8602, Japan
[20] Department of Physics, Princeton University, Princeton, New Jersey, USA
[21] Department of Physics, Purdue University, 525 Northwestern Avenue, West Lafayette, Indiana, USA
[22] Department of Physics, University of California, Berkeley, California, USA
[23] Department of Physics, University of California, One Shields Avenue, Davis, California, USA
[24] Department of Physics, University of California, Santa Barbara, California, USA
[25] Department of Physics, University of Illinois at Urbana-Champaign, 1110 West Green Street, Urbana, Illinois, USA
[26] Dipartimento di Fisica G. Galilei, Università degli Studi di Padova, via Marzolo 8, 35131 Padova, Italy
[27] Dipartimento di Fisica, Università La Sapienza, P.le A. Moro 2, Roma, Italy
[28] Dipartimento di Fisica, Università degli Studi di Milano, via Celoria 16, Milano, Italy
[29] Dipartimento di Fisica, Università degli Studi di Trieste, via A. Valerio 2, Trieste, Italy
[30] Dipartimento di Fisica, Università di Ferrara, via Saragat 1, 44122 Ferrara, Italy
[31] Dipartimento di Fisica, Università di Roma Tor Vergata, via della Ricerca Scientifica 1, Roma, Italy
[32] Discovery Center, Niels Bohr Institute, Blegdamsvej 17, Copenhagen, Denmark
[33] Dpto. Astrofísica, Universidad de La Laguna (ULL), 38206 La Laguna, Tenerife, Spain
[34] European Southern Observatory, ESO Vitacura, Alonso de Cordova 3107, Vitacura, Casilla 19001, Santiago, Chile
[35] European Space Agency, ESAC, Planck Science Office, Camino bajo del Castillo s/n, Urbanización Villafranca del Castillo, Villanueva de la Cañada, Madrid, Spain
[36] European Space Agency, ESTEC, Keplerlaan 1, 2201 AZ Noordwijk, The Netherlands
[37] Harvard-Smithsonian Center for Astrophysics, 60 Garden Street, Cambridge, MA 02138, USA

[38] Helsinki Institute of Physics, Gustaf Hällströmin katu 2, University of Helsinki, Helsinki, Finland
[39] INAF - Osservatorio Astrofisico di Catania, via S. Sofia 78, Catania, Italy
[40] INAF - Osservatorio Astronomico di Padova, Vicolo dell'Osservatorio 5, Padova, Italy
[41] INAF - Osservatorio Astronomico di Roma, via di Frascati 33, Monte Porzio Catone, Italy
[42] INAF - Osservatorio Astronomico di Trieste, via G.B. Tiepolo 11, Trieste, Italy
[43] INAF/IASF Bologna, via Gobetti 101, Bologna, Italy
[44] INAF/IASF Milano, via E. Bassini 15, Milano, Italy
[45] INRIA, Laboratoire de Recherche en Informatique, Université Paris-Sud 11, Bâtiment 490, 91405 Orsay Cedex, France
[46] IPAG (Institut de Planétologie et d'Astrophysique de Grenoble), Université Joseph Fourier, Grenoble 1/CNRS-INSU, UMR 5274, 38041 Grenoble, France
[47] Imperial College London, Astrophysics group, Blackett Laboratory, Prince Consort Road, London, SW7 2AZ, UK
[48] Infrared Processing and Analysis Center, California Institute of Technology, Pasadena, CA 91125, USA
[49] Institut Néel, CNRS, Université Joseph Fourier Grenoble I, 25 rue des Martyrs, Grenoble, France
[50] Institut d'Astrophysique Spatiale, CNRS (UMR8617) Université Paris-Sud 11, Bâtiment 121, Orsay, France
[51] Institut d'Astrophysique de Paris, CNRS UMR7095, Université Pierre & Marie Curie, 98bis boulevard Arago, Paris, France
[52] Institut de Ciències de l'Espai, CSIC/IEEC, Facultat de Ciències, Campus UAB, Torre C5 par-2, Bellaterra 08193, Spain
[53] Institute of Astronomy and Astrophysics, Academia Sinica, Taipei, Taiwan
[54] Institute of Astronomy, University of Cambridge, Madingley Road, Cambridge CB3 0HA, UK
[55] Institute of Theoretical Astrophysics, University of Oslo, Blindern, Oslo, Norway
[56] Instituto de Astrofísica de Canarias, C/vía Láctea s/n, La Laguna, Tenerife, Spain
[57] Instituto de Física de Cantabria (CSIC-Universidad de Cantabria), Avda. de los Castros s/n, Santander, Spain
[58] Jet Propulsion Laboratory, California Institute of Technology, 4800 Oak Grove Drive, Pasadena, California, USA
[59] Jodrell Bank Centre for Astrophysics, Alan Turing Building, School of Physics and Astronomy, The University of Manchester, Oxford Road, Manchester, M13 9PL, UK
[60] Kavli Institute for Cosmology Cambridge, Madingley Road, Cambridge, CB3 0HA, UK
[61] LERMA, CNRS, Observatoire de Paris, 61 Avenue de l'Observatoire, Paris, France
[62] Laboratoire AIM, IRFU/Service d'Astrophysique - CEA/DSM - CNRS - Université Paris Diderot, Bât. 709, CEA-Saclay, 91191 Gif-sur-Yvette Cedex, France
[63] Laboratoire Traitement et Communication de l'Information, CNRS (UMR 5141) and Télécom ParisTech, 46 rue Barrault , 75634 Paris Cedex 13, France
[64] Laboratoire de Physique Subatomique et de Cosmologie, CNRS/IN2P3, Université Joseph Fourier Grenoble I, Institut National Polytechnique de Grenoble, 53 rue des Martyrs, 38026 Grenoble Cedex, France
[65] Laboratoire de l'Accélérateur Linéaire, Université Paris-Sud 11, CNRS/IN2P3, Orsay, France
[66] Lawrence Berkeley National Laboratory, Berkeley, California, USA
[67] Max-Planck-Institut für Astrophysik, Karl-Schwarzschild-Str. 1, 85741 Garching, Germany
[68] MilliLab, VTT Technical Research Centre of Finland, Tietotie 3, Espoo, Finland
[69] National University of Ireland, Department of Experimental Physics, Maynooth, Co. Kildare, Ireland
[70] Niels Bohr Institute, Blegdamsvej 17, Copenhagen, Denmark
[71] Observational Cosmology, Mail Stop 367-17, California Institute of Technology, Pasadena, CA, 91125, USA
[72] Optical Science Laboratory, University College London, Gower Street, London, UK
[73] SISSA, Astrophysics Sector, via Bonomea 265, 34136, Trieste, Italy
[74] SUPA, Institute for Astronomy, University of Edinburgh, Royal Observatory, Blackford Hill, Edinburgh EH9 3HJ, UK
[75] School of Physics and Astronomy, Cardiff University, Queens Buildings, The Parade, Cardiff, CF24 3AA, UK
[76] Space Sciences Laboratory, University of California, Berkeley, California, USA
[77] Spitzer Science Center, 1200 E. California Blvd., Pasadena, California, USA
[78] Stanford University, Dept of Physics, Varian Physics Bldg, 382 via Pueblo Mall, Stanford, California, USA
[79] Université de Toulouse, UPS-OMP, IRAP, 31028 Toulouse Cedex 4, France
[80] Universities Space Research Association, Stratospheric Observatory for Infrared Astronomy, MS 211-3, Moffett Field, CA 94035, USA
[81] University of Granada, Departamento de Física Teórica y del Cosmos, Facultad de Ciencias, Granada, Spain
[82] University of Miami, Knight Physics Building, 1320 Campo Sano Dr., Coral Gables, Florida, USA
[83] Warsaw University Observatory, Aleje Ujazdowskie 4, 00-478 Warszawa, Poland